Marine and Petroleum Geology

Paleo-redox conditions during the demise of a carbonate platform in the Tethyan Ocean: evidence from phosphatized and metals (Mn and Fe) rich hardgrounds

--Manuscript Draft--

Manuscript Number:	JMPG-D-24-01127
Article Type:	Research Paper
Keywords:	Cretaceous carbonate platform; drowning unconformity; Fe-Mn hardground; paleo redox conditions; Raman spectroscopy; climate change; synsedimentary tectonic; Sicily
Abstract:	Phosphatized Mn and Fe rich hardgrounds and condensed pelagic deposits in carbonate platform successions are precious archives of abrupt climate and environmental changes (redox conditions and phosphorous availability) in the past shallow-water marine environment. In this work we study three phosphatized Mn and Fe rich hardgrounds and pelagic condensed deposits that mark the repetitive demise of the Panormide carbonate platform (Southern Tethyan domain) during the Cretaceous. The integration of SEM-EDS, PXRD, and Micro-Raman spectroscopy data shows that these hardgrounds consist of fine-grained Fe (goethite and hematite) and Mn (birnessite and/or vernadite) oxides dispersed in a calcite and apatite matrix. Micro-Raman spectroscopy shows the presence of oxidized Mn species: Mn^{3+} and Mn^{4+}. The oxidation of $Mn^{2+} \rightarrow Mn^{3+/4+}$ and/or $Fe^{2+} \rightarrow Fe^{3+}$ occurred at the sediment-seawater interface under oxic conditions (where both Mn and Fe oxidize) or suboxic conditions (where only Fe oxidizes). Moreover, we show that the formation of the phosphatized metals-rich hardgrounds occurred during long-term periods (6–12 Ma) characterized by negative $\delta^{13}C$ and $\delta^{18}O$ values. The paleoenvironmental perturbations that triggered the formation of both hardgrounds and condensed pelagic deposits were likely related to pCO_2 cycle, upwelling of P-Mn-Fe-rich water masses, and alternation of icehouse to greenhouse conditions characterizing the Cretaceous climate during the considered intervals. These perturbations were likely enhanced by tectonic activity. The paleoenvironmental stresses recorded in the Cretaceous Panormide Southern Tethyan margin can be linked to carbon cycle variations, eutrophication and phosphatization related to the Cretaceous climate oscillations during the main Oceanic Anoxic Events.

Highlights:

Three main phophatized Fe-Mn rich hardgrounds and condensed pelagite couplets interlayered in the Cretaceous shallow-water carbonates

Evaluation of paleo-redox conditions from the Fe-Mn hardgrounds

Paleoenvironmental and paleoclimate changes during the main Cretaceous OAEs

Paleo-redox conditions during the demise of a carbonate platform in the Tethyan Ocean: evidence from phosphatized and metals (Mn and Fe) rich hardgrounds

Luca Basilone[a,b*], Simone Bernardini[c], Fausto Grassa[d], Attilio Sulli[e], Luis M. Nieto[f], Anas Abbassi[c,g], Luigi Jovane[a]

[a] Instituto Oceanográfico da Universidade de São Paulo, Praça do Oceanográfico, 191, São Paulo, SP 05508-120, Brazil

[b] IISS E. Ascione, Via Centuripe 11, 90135 Palermo, Italy

[c]Dipartimento di Scienze, Università di Roma Tre, Largo S. Leonardo Murialdo 1, 00146 Rome, Italy

[d]Istituto Nazionale di Geofisica e Vulcanologia, Sezione di Palermo, Via Ugo La Malfa 153, 90146 Palermo, Italy

[e] Department of Earth and Marine Science, University of Palermo, Via Archirafi 20-22, 90123, Palermo, Italy

[f] Department of Geology and CEACTEMA. University of Jaén. 23071 Jaén, Spain

[g] Laboratory of Research and Development in Applied Geosciences (RDGA), FST-Tanger, University Abdelmalek Essaâdi-Morocco

* Corresponding author (luca.basilone03@gmail.com)

Abstract

Phosphatized Mn and Fe rich hardgrounds and condensed pelagic deposits in carbonate platform successions are precious archives of abrupt climate and environmental changes (redox conditions and phosphorous availability) in the past shallow-water marine environment.

In this work we study three phosphatized Mn and Fe rich hardgrounds and pelagic condensed deposits that mark the repetitive demise of the Panormide carbonate platform (Southern Tethyan domain) during the Cretaceous. The integration of SEM-EDS, PXRD, and Micro-Raman spectroscopy data shows that these hardgrounds consist of fine-grained Fe (goethite and hematite) and Mn (birnessite and/or vernadite) oxides dispersed in a calcite and apatite matrix. Micro-Raman spectroscopy shows the presence of oxidized Mn species: Mn^{3+} and Mn^{4+}. The oxidation of $Mn^{2+} \rightarrow Mn^{3+/4+}$ and/or $Fe^{2+} \rightarrow Fe^{3+}$ occurred at the sediment-seawater interface under oxic conditions (where both Mn and Fe oxidize) or suboxic conditions (where only Fe oxidizes). Moreover, we show that the formation of the phosphatized metals-rich hardgrounds occurred during long-term periods (6–12 Ma) characterized by negative $\delta^{13}C$ and $\delta^{18}O$ values. The paleoenvironmental perturbations that triggered the formation of both hardgrounds and condensed pelagic deposits were likely related to pCO_2 cycle, upwelling of P-Mn-Fe-rich water masses, and alternation of icehouse to greenhouse conditions characterizing the Cretaceous climate during the considered intervals. These perturbations were likely enhanced by tectonic activity. The paleoenvironmental stresses recorded in the Cretaceous Panormide Southern Tethyan margin can be linked to carbon cycle variations, eutrophication and phosphatization related to the Cretaceous climate oscillations during the main Oceanic Anoxic Events.

Keywords: Cretaceous carbonate platform, drowning unconformity, Fe-Mn hardground, paleo redox conditions, C and O isotopes, Raman spectroscopy, climate change, synsedimentary tectonic, Sicily

1. Introduction

Marine ferromanganese crusts consist of Mn and Fe oxyhydroxides precipitating directly from ocean water over hard rock substrates (Hein and Koschinsky, 2014). They form on the flanks and summits of seamounts, ridges, and plateaus where the currents have kept the rocks swept clean of sediments (Segl et al., 1984; De Carlo, 1991). These mineralizations represent the most important polymetallic deposits on seamounts in the central and western Pacific Ocean – notable examples are those of guyots of the Mid-Pacific Mountains (De Carlo, 1991; Wen et al., 1997) –, Mid-Atlantic ridge (Mills et al., 2001), Canary Islands (Kfouri et al., 2021), Lion seamount (Koschinsky et al., 1996) and Cadiz Contourite Channel (González et al., 2012) in the NE Atlantic Ocean.

A fundamental geochemical property of Mn and Fe (the most common metals on Earth) is their high sensitivity to redox conditions. For instance, the solubility of Mn is much higher than that of Fe when the pH ranges from 6 to 8, except at high oxidation/reduction potential (Eh > 600 mV) (Hem, 1963, 1972). Therefore, the geochemical separation between these metals can be used to identify different redox environments and to investigate the evolution of the seawater chemistry over geological time (Berner, 1981; Maynard, 2010; Kfouri et al., 2021). Moreover, in the crystal structures of oxide minerals, Mn may occur under different oxidation states (Mn^{2+}, Mn^{3+}, and Mn^{4+}) depending on the (bio)geochemical conditions existing during mineral formation (*e.g.*, Bernardini et al., 2021a). Marine Fe-Mn deposits are thus precious archives of regional and global oceanic and climatic conditions (Hein and Koschinsky, 2014; Koschinsky and Hein, 2017; Benites et al., 2020; Sutherland et al., 2020).

Phosphorus is an essential nutrient for life and a limiting element for ocean productivity; thus, its availability can strongly influence the marine carbon cycle and the sequestration of atmospheric CO_2 (Paytan and McLaughlin, 2007). The formation of phosphatized hardgrounds in shallow-marine environments can be related to both continental weathering and/or upwelling of P-rich deep waters. For instance, at seamounts/plateaus, the formation of phosphates (*e.g.*, carbonate fluorapatite) in the sediments/rocks commonly occurs at depths where the seafloor intersects the oxygen minimum zone (OMZ) which is a source of reactive P and metals (Kraal et al., 2012). Phosphogenesis may be thus accompanied by the precipitation of Fe and Mn oxyhydroxides, depending on the redox condition of seawaters (Baturin, 1989; Benninger and Hein, 2000).

The demise and drowning of carbonate platform are commonly associated with the formation of Fe and Mn rich levels, phosphatized hardgrounds, pelagic condensed deposits, and changes in the ecology of carbonate-producing organisms. These events thus record the paleoclimate changes (Föllmi et al., 1994; Peter and Simo, 1997; Godet, 2013), as well as the tectonic subsidence and sea-level rises (Schlager, 2005; Nieto et al., 2014; Basilone, 2020) that triggered changes of shallow-water carbonate productivity.

In the Mesozoic Tethyan geological record, Fe-Mn rich levels and drowning unconformities widely occur in different chronostratigraphic intervals. For example, Fe-Mn rich layers and condensed sedimentation (*i.e.*, Rosso Ammonitico), related to the paleoclimatic and paleoenvironmental changes occurring during the Tethyan rifting (Jurassic), have been described from Subbetic (Nieto et al., 2014; Reolid and Abad, 2019), Alpine (Cronan et al., 1991; Vörös, 2012; Godet, 2013), Apennine (Santantonio, 1993; Clari et al., 1995) and western Sicily (Mallarino et al. 2002, Wendt, 2017; Basilone, 2011). Paleoenvironmental perturbations during the Cretaceous produced Fe-Mn levels, pelagite intercalations, facies changes in shallow-water successions and drowning of Northern Tethyan carbonate platforms (Peter and Simo, 1997; Wissler et al., 2003) and Southern Tethyan margin (Immenhauser et al., 2005; Parente et al., 2007; Graziano, 2013; Basilone, 2021a; 2021b). These events are related to the climatic changes producing the Oceanic Anoxic Events (OAE) and biotic extinctions (Larson and Erba, 1999), as demonstrated by the several geochemical, biostratigraphic, and sedimentological analyses of worldwide pelagic successions (Arthur et al., 1990; Menegatti et al., 1998). They record periods of global warming (greenhouse conditions) genetically linked with changes of the pCO_2 of the hydrosphere-atmosphere system, the latter related the tectonic and volcanic processes acting at a global scale (Vogt, 1989; Tarduno et al., 1991; Weissert and Erba, 2004; Tejada et al., 2009; Méahy et al., 2009).

Although these mineralizations are precious archives of the environmental perturbations characterizing the stage of demise and drowning of carbonate platforms, they still remain poorly studied. The lack of data is mainly due to the challenging characterization of fine-grained mixtures of poorly-crystalline Mn and Fe compounds, carbonates, silicates, and phosphates by standard X-ray diffraction methods. Raman spectroscopy provides a valuable tool for characterizing Mn- and Fe-bearing mixtures (Bernardini et al., 2019), being sensitive to short-range cation-anion arrangements. Moreover, the laser spot on the sample can be reduced to ~1 μm^2 allowing for high spatial resolution chemical analysis (Bernardini et al., 2021a; Kfouri et al., 2021). Beside the mineral identification, Raman spectroscopy provides a quick and reliable determination of the oxidation state of Mn down to the microscale (Bernardini et al., 2021b) thus allowing the use of these minerals for paleoenvironmental reconstructions (Bernardini et al., 2021a; Kfouri et al., 2021).

In this paper we provide a detailed sedimentological, stratigraphical and mineralogical description of three phosphatized MnFe-rich hardgrounds associated with discontinuous and condensed sediments, firstly recognized in the Cretaceous shallow-water carbonates of the Panormide Southern Tethyan domain (NW Sicily, Fig. 1a). These hardgrounds were studied by combining Optical Microscopy (OM), Scanning Electron Microscopy coupled with an X-ray Energy Dispersive System (SEM-EDS), Powder X-Ray Diffraction (PXRD), and Micro-Raman spectroscopy (RS). The aim of this work is at providing insights into the paleoclimate changes of a shallow-water marine environment triggering the repetitive demise of a carbonate platform in the Southern Tethyan margin.

2. Geological setting

Sicily is a segment of the Apenninic-Tyrrhenian System African Maghrebides (inset in Fig. 1a) whose upbuild refers to both the convergence between Africa and a complex "European" crust (Bonardi et al., 2001) and to the coeval roll-back of the subduction hinge of the Adriatic Ionian-African lithosphere (Chiarabba et al., 2008). The Sicily chain is a S- and SE-verging, up to 15 km thick, fold and thrust belt (FTB) involving Meso-Cenozoic carbonate and siliciclastic units, overthrusting the Iblean foreland (Finetti et al., 2005; Catalano et al., 2013a; Henriquet et al., 2020). Its formation was associated with the counter-clockwise rotation of Corsica and Sardinia and the Calabrian/Peloritani Kabylian units, during the late Neogene (Channell et al., 1990). Thrust-top basins grew above the deforming units during the Late Miocene, when clastics and Messinian evaporites were deposited, sealing unconformably the deformed units (Gasparo Morticelli et al., 2015). A thick-skinned thrusting in the frontal area of the Sicilian FTB as well as the crystalline basement in the inner and deeper sector of the chain involve Plio-Pleistocene deposits (Sulli et al., 2021). Quaternary deposits, outcropping in thin and patchy exposed successions mostly along the coastal belt (Fig. 1a, Agate et al., 2017) and made up of continental (aeolian, debrites, alluvium) and shallow-water carbonate marine deposits, are bounded by unconformity surfaces with regional extension (Di Maggio et al., 2009).

The Palermo Mountains, representing the north-westernmost sector of the outcropping Sicilian FTB, result from the piling-up of shallow-water and deep-water carbonate tectonic units (Fig. 1a, Servizio Geologico d'Italia, 2011a, 2011b), deriving from the deformation of the Panormide carbonate platform and Imerese basin respectively, which developed during the Meso-Cenozoic along the Southern Tethyan stretched continental margin (Catalano et al., 1996). The carbonate platform tectonic units, 800-1200 m-thick and 3-8 km^2 wide, are progressively superimposed along N-S and NW-SE trending thrusts, with ramp and flat geometry (Fig. 1b). The tectonic units are separated by the Oligo-Miocene Numidian flysch deposits that postdate the tectonic emplacement (Catalano et al., 2013b, 2013c). Recent extensional and transtensional tectonic dissect, with E-W oriented and N to S dipping faults, the previously formed structures, being responsible for the present-day morpho-structural setting (Fig. 1a, Di Maggio et al., 2017).

2.1. Main stratigraphy and paleogeography of the Panormide carbonate platform

The Panormide succession outcropping in the Palermo Mountains consists of Upper Triassic-Eocene carbonates, mostly characterized by shelf facies with rimmed margin (Late Triassic and Late Jurassic: Catalano et al., 2013b, 2013c; Basilone and Sulli, 2016) and open platform with ramp geometries (Cretaceous and Eocene: Di Stefano and Ruberti, 2000; Basilone and Di Maggio, 2016). Common fossils include corals, sponges, hydrozoans, rudists and large benthic foraminifera. Several formations, recently revised and amended (Catalano et al., 2013b, 2013c; Basilone, 2018), compose the lithostratigraphic column reconstructed for the study area (Fig. 1c). Paleoenvironmental reconstruction refers the deposits of the Panormide to a Bahamian-type carbonate platform flanked northwards (present-day) by deep-water areas (Catalano et al., 1996). At the Sinemurian-Pliensbachian boundary, the latest stage of rifting, the Triassic-Lower Jurassic wide carbonate platform was tectonically dismembered and consequently drowned (Jenkyns, 1970). During the Jurassic and the Cretaceous the paleophysiography of the Sicilian margin was characterized by shelf areas alternated with several small intraplatform basins (Catalano et al., 2000), frequently associated with strike-slip movements (Basilone, 2022) and emerged areas with continental deposits (*i.e.*, subaerial exposure: Zarcone and Di Stefano, 2010; Basilone et al., 2017).

3. **Methodologies**

Several thin sections have been studied by OM for the analysis of fossil content and textural features, applying microfacies Dunham classification (Dunham, 1962). The resulting lithofacies were calibrated by using biostratigraphic data, mostly based on algae and benthic foraminifera biozonations (Fig. 2), coming from studies on Sicilian (Montanari, 1965; Camoin, 1983), Southern Apennine (De Castro, 1991; Chiocchini et al., 2008), and Adriatic (Husinec and Sokač, 2006; Velić, 2007) successions. Pelagic intercalations were age-calibrated by using calpionellid (Allemann et al., 1971; Remane, 1998) and planktonic foraminifera (Caron, 1985) biozonations. The numerical age of the sedimentary bodies refers to the official chronostratigraphic scale (Cohen et al., 2013).

SEM-EDS data were collected at DAFNE-L (Istituto Nazionale di Fisica Nucleare, INFN) in Frascati (Rome, Italy) using a SNE3200M microscope, equipped with a high-resolution energy-dispersive (EDS) Bruker detector (XFLASH Detector 410 M) and the ESPRIT 1.9 software.

PXRD data were collected at CORE-Laboratory (University of São Paulo, Brazil) using a Siemens D5000 powder diffractometer under CuKα radiation filtered by a monochromator graphite crystal in the 5 – 70° 2θ range, with a step size of 0.02° 2θ, and a counting time of 4 s/step.

Raman measurements were performed at the Raman Spectra Lab, Department of Science, Roma Tre University, at room temperature using an inVia Renishaw spectrometer equipped with a diode laser (532 nm, output power 100 mW), an edge filter, a 1800 lines per mm diffraction grating and a Peltier cooled 1024 × 256 pixel CCD detector. Samples were mounted on the manual stage of a Leica DM2700 M confocal microscope. Focusing of the laser beam and collection of Raman scatterings was realised by a 50X long-working distance objective. The spectra were collected using a laser power of 0.5 mW (three accumulations, 30 s each) in order to avoid any laser-induced degradation of the sample (Bernardini et al., 2020, 2023). The Raman spectrometer was calibrated prior to the measurements using a Si wafer. Spectra acquisition and data analyses were accomplished using WiRE™ and OriginPro software. The measured spectra were baseline-corrected and fitted with pseudo-Voigt functions to derive the phonon wavenumber. The peak positions are estimated to be accurate to at least ± 2 cm^{-1}.

Stable isotopes (C and O) analyses of the micritic component collected from the polished slabs with a micro drill were carried out at the Stable Isotope Laboratory of the INGV (Palermo), using Analytical Precision AP 2003 and FinniganMAT Delta Plus IRMS devices. The results were calibrated to the VPDB standard, with a precision better than 0.1‰ for both C and O isotope compositions.

4. Results

4.1. *Lithostratigraphy and facies analysis*

The 250-500 m-thick Upper Jurassic-Upper Cretaceous study section (Fig. 3), consist of shallow-water carbonates, divided into three lithostratigraphic units (Figs. 1c and 2; Table 1): (1) the Calcari di Pizzo Manolfo (hereafter Gastropod Limestone), (2) the Calcari di Capo Gallo (Requienid Limestone) and (3) the Pellegrino Fm (Rudistid Limestone). Upwards, the series ends with pelagic carbonates belonging to the Amerillo Fm.

The Gastropod Limestone (Fig. 1c) displays shallowing upward cycles of grey thick-bedded bioclastic wackestone-packstone with diceratids and nerineids, thin light grey fenestral limestone, and cm-thick graded oolitic and bioclastic packstone-grainstone (Table 1). The fossil content constraints these carbonates to the Late Tithonian-Berriasian (Fig. 2).

The Requienid Limestone (Fig. 1c) consists of deepening upward cycles of m-thick dark-grey graded floatstone and wackestone-packstone, with bioclasts and coated grains, alternated with darkish oolitic and bioclastic packstone-grainstone with abraded and broken ooids and cm-thick laminated wackestone-packstone with fenestrae, peloids and algal fragments. The fossil content, among which requienids, large gastropods, benthic foraminifera, corals, and green algae with additional contribution from microbial nodules and crusts (Table 1) constraints these beds to Barremian-lower Aptian (Fig. 2).

The Rudistid Limestone (Fig. 1c) features shallowing upward cycles of thick-bedded massive floatstone-wackestone and boundstone with rudistids, corals and benthic foraminifera, along with graded packstone-grainstone and darkish oolitic grainstone (Table 1). The fossil evidence dates these deposits to the upper Albian-Cenomanian (Fig. 2).

The Amerillo Fm (Fig. 1c) includes thin-bedded white, grey and reddish planktonic foraminifera-bearing mudstone-wackestone, with intercalations of bioclastic packstone containing bryozoan and calcareous algae fragments (Table 1). This unit, which follows in onlap and infilling geometry the older Rudistid limestone, is dated uppermost Cretaceous-Paleogene (Fig. 2).

4.2. *Unconformities and associated condensed deposits*

The described shallow-water units are separated by unconformities (DUs in Fig. 3) associated with dm-thick condensed sections (CSs in Fig. 3). The unconformities are submarine erosional surfaces (Figs. 4a, 4c and 4e). The condensed sections are made up of blackish/reddish hardgrounds (HGs in Fig. 3), which directly overlie the previously eroded shallow-water deposits, and by a package of condensed pelagites (CPs in Fig. 3). Mineralization also fills neptunian dykes along orthogonal fractures and stratabounds (Fig. 4b).

The lowermost condensed section (CS1 in Fig. 3) marks the boundary between the Gastropod Limestone and the Requienid Limestone (Fig. 4a). The CS1 thick-bedded package (30-80 cm-thick) consists of two hardgrounds (HG1a and HG1b in Figs. 3 and 4a) alternating with condensed pelagites (CP1 in Fig. 3 and layers a-f in Fig. 4a). HG1a is a 2-6 cm-thick blackish massive crust draping the top of the shallow-water deposits (*i.e.*, the Gastropods limestone, GAS in Fig. 4a). HG1b is a 8-10 cm-thick brick red massive and laminated crust (Fig. 4a). The condensed pelagites comprise graded and planar laminated bioclastic grainstone-to-packstone with reworked shallow-water intraclasts, recrystallized thick-shelled mollusc fragments, crinoids and echinoids (layer a in Fig. 4a, and Fig. 5a) and red to grey massive wackestone-mudstone (layers b-c in Fig. 4a) with thin-shelled molluscs (filaments), *Protopeneroplis trochangulata* Septfontaine, *Salpingoporella* sp., sponge spiculae, calcitized radiolarians, and *Calpionellites darderi* Colom (Fig. 5b). White and greyish reverse graded and planar- to oblique-laminated wackestone with thin-shelled bivalve and gastropod fragments (layers d-e-f in Fig. 4a) rests on the HG1b. On the basis of the fossil content and stratigraphic constraints we can refer the CS1 to the Valanginian-Hauterivian time interval (8-10 Ma). In detail, the unconformity surface formed at the Berriasian/Valanginian boundary (DU1 in Fig. 3). The immediately overlying hardground (HG1a) and the pelagites with calpionellids (layers a-c in Fig. 4a) belong to the lower Valanginian, based on the *Calpionellites darderi* biozone (Fig. 2). The upper laminated pelagites (layers d-f in Fig. 4a), lacking calpionellids due to their extinction at the early/late Valanginian boundary (Allemann et al., 1971; Remane, 1998), were deposited in the late Valanginian-Hauterivian time interval, capped by the Barremian Requienid Limestone (REQ in Fig. 4a). Consequently, the hardground HG1b, interlayered between the two pelagic horizons, can be assigned to the early/late Valanginian boundary.

The intermediate condensed section (CS2 in Fig. 3) marks the boundary between the Requienid Limestone (Barremian-lower Aptian) and the Rudistid Limestone (Upper Albian-Cenomanian). It consists of a 10-20 cm-thick massive reddish hardground (HG2 in Figs. 3 and 4c), draping the Requienid Limestone along an irregular bio-eroded surface (DU2 in Figs. 3), with infilling geometries, and 5-20 cm-thick of red to yellowish pelagic carbonates (CP2 in Figs. 3 and 4c). The pelagites include bioclastic and intraclastic laminated wackestone with aligned thin-shelled bivalve fragments, sponge spiculae, radiolarians and strongly recrystallized planktonic foraminifera (Fig. 5c). Upwards, a sharp surface with downlap stratal terminations marks the boundary with the younger Rudistid Limestone (RUD in Fig. 4c). Since the DU2 unconformity marks the top of the Barremian-lower Aptian carbonate platform, the hardground (HG2) and the overlying condensed pelagites (CP2) are stratigraphically assigned to the upper Aptian-lower Albian time interval (10-15 Ma).

The uppermost condensed section (CS3 in Fig. 3) consists of two thin reddish hardgrounds (HG3a and HG3b in Figs. 3 and 4e) interlayered with condensed pelagites (CP3 in Figs. 3 and

4e). HG3a, marking the upper boundary of the Cenomanian Rudistid limestone (RUD in Fig. 4e), is a mm-thick oxide encrustation, developing over irregular dissolution surface (Fig. 5d). The condensed pelagites are made up by dm-thick packstone with planktonic foraminifera and wackestone-packstone with abundant thin-shelled bivalves and planktonic foraminifera (*Hedbergella* sp., rotalipods). The latter show planar and oblique lamination (Fig. 5f) and laterally drape the RUD with infilling geometry. Upwards, the HG3b cm-thick reddish hardground lies immediately below the white and reddish Late Cretaceous (Campanian-Maastrichtian)-Eocene planktonic foraminifera-bearing wackestone of the Amerillo Fm (AMM in Fig. 4e). Assuming the unconformity (DU3 in Fig. 3) formed at the Cenomanian/Turonian boundary (Fig. 2), the CS3 can be assigned to the Turonian-Early Campanian time (ca. 10 Ma).

4.3. *Synsedimentary tectonic*

A common feature characterizing the topmost portion of the three shallow-water units is the occurrence of synsedimentary normal faults and of a metre-scale dense network of neptunian dykes and enlarged fractures (Fig. 4b). The synsedimentary faults, NNE-SSW oriented and variously dipping (ENE and WSW), cut the top of the shallow-water units with small downthrown; they are sealed by the hardgrounds (HGs) and the pelagites (CPs) that, locally, display onlap and buttress unconformity relationships (Fig. 4a). The neptunian dykes, both bed-parallel and vertical to the bedding, and large (some decimetres wide) to small dissolution cavities (Fig. 4d) are also filled by the hardgrounds and pelagites (Fig. 4b).

4.4. *Mineralogy of the phosphatized FeMn-rich hardgrounds*

Preliminary OM examination of the HGs hardgrounds shows that they consist of blackish-to-reddish grains (with a size of few microns) finely dispersed within a calcite-rich matrix (Fig. 5d) or encrusting fractures/fissures, dissolution cavities, and stylolite surfaces (Figs. 5e-f).

SEM-EDS chemical maps collected from samples of all hardgrounds show that the µmsized blackish-to-reddish grains in the calcite matrix are rich of Fe (red grains in Fig. 6a). Notably, in the HG1a and HG1b levels the Fe-grains are finely intermixed with Mn-rich grains (Figs. 6b). Single point EDS spectra collected from the Mn-grains show the occurrence of other metals: Co, Ni, and Cu (Fig. 6c).

PXRD data collected from the three hardgrounds yielded sharp Bragg peaks of calcite and carbonate fluoro-apatite (Ca and CFA in Fig. 7, respectively). Notably, the uppermost hardgrounds (HG3a and HG3b) show the highest content of CFA (see the strong reflection at ~ 32° 2θ, Fig. 7). Additional weak and broad peaks of poorly-crystalline goethite [FeOOH] have been identified in the patterns collected from the samples HG1a, HG1b, and HG2 (see the weak reflection at ~ 21° 2θ in Fig. 7).

Raman spectra show the presence of different Fe compounds in all HGs hardgrounds: hematite [Fe_2O_3] characterized by peaks at ~ 223, 293, 407, 655 and 1315 cm^{-1} (spectrum S1 in Fig. 8), goethite (S2 in Fig. 8) with peaks at ~ 300, 394, 480, 553 cm^{-1} (de Faria et al., 1997); finally, a band at ~ 685 cm^{-1} in spectrum S2 suggests the possible presence of magnetite [Fe_3O_4] (de Faria et al., 1997). Mn oxide(s) have been identified in samples from HG1a-b hardgrounds by bands at ~ 399, 500, 580, 630, and 735 cm^{-1} (S3 in Fig. 8). These spectral features are consistent with the mineral birnessite [a Mn oxide with a layer structure and ideal formula (Na, Ca, K)(Mn^{4+}, Mn^{3+})$_2O_4 \cdot 1.5H_2O$] or vernadite (Bernardini et al., 2019; Julien et al., 2003), a z-disordered variety of birnessite. Based on the data of Bernardini et al. (2021), in these compounds Mn occurs as Mn^{3+} (strong scattering ~ 580 cm^{-1}) and Mn^{4+} (scattering at ~ 630 cm^{-1}, see Fig. 8).

A summary of the mineralogical results is provided in Table 2.

4.5. *Carbon and Oxygen isotope analysis*

The evolution of carbon and oxygen isotopic composition along the three condensed sections CSs (Fig. 3) comprising the hardgrounds and the condensed pelagites is given in Figure 9.

In the lower condensed section (CS1), the $\delta^{13}C$ curve (average value 0.35 ‰) is characterised by a sharp negative shift (from ~ 1.5 ‰ to -3.49 ‰) approaching the HG1b hardground (Fig. 9). A subsequent positive shift towards ~ 2.7 ‰ is observed in the uppermost CP1 pelagic horizon (Fig. 9). The $\delta^{18}O$ (average value -2.32 ‰) shows a similar trend: it reaches its minimum value in the HG1b hardground (-4.49 ‰, Fig. 9) and increases up to -0.12 ‰ in the upper CP1 horizon (Fig. 9). No clear perturbation of $\delta^{13}C$ and $\delta^{18}O$ is observed in the HG1a hardground (Fig. 9).

A similar variation is observed in the intermediate condensed section (CS2 in Fig. 9); the $\delta^{13}C$ record shows values between 2.44 ‰ and -3.97 ‰ (average value 0.23 ‰), reaching the minimum values (-3.97 ‰) in the HG2 hardground (Fig. 9). A subsequent positive shift to 1.93 ‰ is observed toward the CP2 horizon (Fig. 9). In this interval, the $\delta^{18}O$ isotope data range from -4.84 to -1.47 ‰ (average value -2.66 ‰), reaching its minimum value in the HG2 hardground (Fig. 9) and increasing in the upper pelagic horizon (CP2 in Fig. 9).

In the uppermost condensed section (CS3 in Fig. 9) the $\delta^{13}C$ record shows values between 2.70 ‰ and -1.84 ‰ (average value 1.37 ‰). In the lowermost part of the section (*i.e.*, the top of the shallow-water Rudistid Limestone, RUD in Fig. 9), $\delta^{13}C$ values range between 0.86 ‰ and 2.15 ‰ (Fig. 9) and then decrease in the lowest phosphatized HG3a hardground (Fig. 9). The $\delta^{13}C$ reach the maximum value (2.70 ‰) in the following thin pelagic horizon (CP3, Fig. 9) and then shift to -1.84 ‰ in the HG3b hardground (Fig. 9). Finally, the $\delta^{13}C$ increases up to 2.52 ‰ in the planktonic foraminifera-bearing wackestone of the Amerillo Fm (Fig. 9). The $\delta^{18}O$ record range from -0.50 to -3.98 ‰ (average value -1.94 ‰). The $\delta^{18}O$ increases from -3.11 to -0.50 ‰ approaching the lower phosphatized HG3a hardground (Fig. 9), where it decreases to -2.04 ‰ (Fig. 9). The $\delta^{18}O$ increases up to -0.50 ‰ in the upper pelagic (CP3) horizon (Fig. 9) and decreases to -3.98 ‰ within the HG3b hardground (Fig. 9). Similarly to what observed for the $\delta^{13}C$ curve, the $\delta^{18}O$ shows a gradual increasing trend towards positive values in the pelagites of the Amerillo Fm (Fig. 9).

5. Discussion

Three phosphatized metal-rich hardgrounds (HGs in Fig. 3) associated with unconformity surfaces and condensed pelagic deposits (DUs and CPs in Fig. 3) mark repetitive episodes of shallow-water carbonate production shutdown in the Tethyan Ocean during the Cretaceous.

Textural features and fossil assemblages in the condensed pelagic deposits overlying each carbonate platform unit (Figs. 3, 4, 5) record strong environmental changes with the development of open-sea conditions that are the typical characteristics of drowning unconformities (*e.g.*, Schlager, 1981; Godet, 2013). These features highlight cyclic episodes of demise and rebirth of the carbonate platform (*e.g.*, Reolid and Abad, 2019; Danisch et al., 2021).

The lowermost demise event (DU1/CP1 in Figs. 3 and 10) encompasses a long-time period: from the demise of the carbonate platform at Berriasian/Valanginian boundary to its rebirth since the Barremian. This event is coeval with other demise and drowning events recorded along many Tethyan carbonate platforms (Fig. 10, Simo et al., 1993; Van de Schootbrugge et al., 2003). The sharp positive-to-negative excursions of the Valanginian-Hauterivian $\delta^{13}C_{bulk}$ pattern of the Colombrina section (HG1b in Fig. 9), which are in agreement with the shallow- and deep-water reference sections from the Tethyan domain (McArthur et al., 2007; Westermann et al., 2010; Charbonnier et al., 2013; Lukeneder et al., 2016; Grădinaru et al., 2016; Aguado et al., 2018), provide a solid evidence for the chronostratigraphic assignment of the study interval to the drowning of many carbonate platforms that prelude the onset of the "Weissert Event".

The intermediate demise event (DU2/CP2 in Fig. 3) occurred at end of the lower Aptian Requienid Limestone sedimentation. The condensed pelagites (CP2) and phosphatized Fe-rich hardground (HG2) are capped by the uppermost Albian-Cenomanian Rudistid Limestone (Fig. 3). This event is coeval with the drowning events widely recognized in the peri-Tethyan carbonate platforms (Fig. 10; Simo et al., 1993; Föllmi and Gainon, 2008; Graziano, 2013; Westermann et al., 2013; Huck et al., 2013). Drowning events and phosphatized deposits observed in other Tethyan and North Atlantic carbonate platforms were related to flooding of carbonate platforms by nutrient-rich waters during enhanced burial of organic matter and acidification of the oceanic waters (Föllmi et al., 1994; Weissert et al., 1998; Föllmi and Gainon, 2008). These events correspond with the global perturbations of CO_2 and correlated with the onset of the OAEs, among them the so called "Selli level" (Fig. 10, Menegatti et al., 1998; Jenkyns, 2018). Uplift and kaolinitic clays deposition in other Panormide platform blocks (Basilone et al., 2017) suggest that the eutrophication was likely fuelled by enhanced continental weathering (*e.g.*, clastic influx from continental areas).

The uppermost drowning event (DU3/CP3 in Fig. 3) occurs at the end of the Cenomanian shallow-water sedimentation. The overlying pelagites and the phosphatized Fe-rich hardground (CP3 and HG3b in Fig. 3) are capped by the Upper Campanian-Paleogene pelagic limestone (AMM), which reveals the definitively drowning of the whole Panormide carbonate platform. This event coincides with the drowning and/or long-term uplifting events described from Sicily, Southern Apennines and Apulia carbonate platforms (Fig. 10; Mindzenty et al., 1995; Carannante et al., 2008; Basilone and Sulli, 2018), some of which were related with the onset of the OAE2 "Bonarelli level" (Fig. 10; Parente et al., 2007).

Among the several mechanisms proposed to explain the demise of carbonate platforms and the generation of a drowning unconformity, rapid tectonic collapse of the platform, sea-level rise, upwelling of anoxic deep-ocean waters, and/or climate changes are the most accepted (*e.g.*, Dromart et al., 2003; Mutti and Bernoulli, 2003; Brandano et al., 2016). The occurrence, just below of each unconformity, of enlarged fractures, normal faults, open spaces, collapse phenomena, and neptunian dykes (Figs. 4b-d) suggests fracturing in an overall tensional regime (Bourrouhil et al., 1998; Wendt, 2017) and dislocation of an already hardened substrate (James and Choquette, 1983) in faulted-platform blocks (see Santantonio, 1993; Bosence, 2005; Nieto et al., 2014, Basilone, 2020). The low rates of tectonic subsidence for the Colombrina block during the considered intervals (see Basilone, 2021b) and the "rapid" facies changes from demise to rebirth of the carbonate platform suggest that the perturbation resulted from nutrient excess or eutrophication in shallow water followed by deepening at shallow depths (*e.g.,* Mallarino et al., 2002).

Episodes of paleoenvironmental stress trigger reduction or halt in shallow-water carbonate production. Sea-surface water temperature directly drives the ecology and morphology of carbonate platforms (Lees and Buller, 1972; Pomar 2020). Thus, changes in sea-surface water temperatures (Jenkyns and Wilson, 1999) or in detrital fluxes and flooding of platforms by nutrient-rich waters frequently cause the eutrophication of the carbonate system and a drastic reduction of its growth potential (Föllmi, 2012). One of the most important factors causing changes of sea-surface ocean water chemistry is the increase of dissolved CO_2 contents in the hydrosphere/atmosphere system, which induces lower pH values, producing the so-called "ocean acidification" (Kleypas et al., 1999; Orr et al., 2005).

The abundant CFA identified by PXRD and SEM-EDS in the metal-rich hardgrounds (*i.e.,* mostly in the HG3a-b, see Figs. 6 and 7) in the Colombrina section suggests that the demise events occurred during high nutrients supply. Under high phosphate levels, nutrient conditions became eutrophic and the platform ecosystem stop producing carbonate, leading to platform demise (*e.g.,* N Tethyan margin; Föllmi and Godet, 2013; Chatalov et al., 2015). Phosphorus is primarily delivered to marine surface waters *via* continental weathering (riverine influx) and upwelling of deep waters (Paytan and McLaughlin, 2007). Therefore, the repetitive demise of the Panormide carbonate platform can be linked with episodic enrichment of phosphorous resulting from increased continental weathering and/or upwelling of deep-water masses; the latter process likely favoured by palaeoceanographic and tectonic settings. Notably, episodic upwelling of cold and nutrient-rich waters has been related to development of phosphatized hardgrounds on several Miocene carbonate platforms (Mutti and Bernoulli, 2003; Brandano et al., 2016).

5.1. *Redox conditions and paleoclimatic implications*

In the scenario depicted above, the episodic perturbations in the redox conditions during the demise events and the repetitive phosphatization of the platform seafloor may have been recorded by the redox-sensitive (Mn and Fe) metals. Notably, our SEM-EDS, PXRD and RS data show the separation between Mn and Fe in the different phosphatized hardgrounds (HGs). The HG1a-b hardgrounds, formed during the lowermost demise event (Valanginian – Hauterivian, see Fig. 11a), are rich of Mn and Fe (see Fig. 6b) and consist of a very fine mixture of Mn oxides with a layer structure (birnessite and/or its disordered variety vernadite), Fe oxides (goethite, hematite, and minor magnetite), calcite, and CFA (see Table 2). Notably, vernadite is a common mineral in marine ferromanganese deposits that typically precipitates under oxic conditions directly from ocean water (hydrogenesis) onto hard rock substrates (see Hein and Koschinsky, 2014 for a detailed explanation). This genetic process is also consistent with the identification of abundant goethite, a compound that can be interpreted as the final product of hydrogenetic Fe^{2+} to Fe^{3+} oxidation (Hein et al., 2000). In marine environment, Mn and Fe oxides concentrate different critical elements from seawater (*e.g.*, Co, Ti, Li, Pt, Zr, Nb, Te, Ni, V, Bi, Mo, W, among others), depending on the water (redox) conditions (Hein et al., 2000). For example, Co, Te, and Ce are the most characteristic metals of hydrogenetic precipitation (under oxic conditions) while Ni, Cu, Li, and Zn (which are produced by dissolution of redox-sensitive components in the sediment) are typical of diagenetic precipitation under suboxic conditions (Hein and Koschinsky, 2014). EDS data revealed that the birnessite/vernadite grains are rich of Cu, Ni, and Co (Fig. 6c). The identification of trace metals characteristic of both hydrogenetic (Co) and diagenetic (Cu and Ni) precipitation is consistent with the oxidation of Mn at the seawater-sediment interface (Fig. 11a). Moreover, analysis of the Raman spectra revealed the presence of oxidized Mn species: Mn^{3+} and Mn^{4+} (see Fig. 8). Altogether these results suggests that the oxidation of Fe^{2+} to Fe^{3+} and Mn^{2+} to $Mn^{3+/4+}$ during the DU1/CP1 event occurred onto the seafloor under oxic seawater conditions (Fig. 11a).

A slightly different scenario can be proposed for the intermediate demise (Aptian-Albian) and uppermost drowning (Turonian-Campanian) events (DU2/CP2 and DU3/CP3 in Figs. 11b and 11c). Our data show that the HG2 and HG3a-b hardgrounds are free of Mn (see Fig. 6) and (similarly to the HG1a-b hardgrounds) consist of a fine mixture of goethite, hematite, magnetite, calcite, and CFA (Table 2). The important point here is that Mn has higher solubility than Fe when the pH is between 6 and 8, except at high Eh (above 600 mV) (Hem, 1963, 1972). Our results thus suggest that the formation of Fe oxides during these events (DU2/CP2 and DU3/CP3) occurred under suboxic conditions in which Fe^{2+} oxidizes to Fe^{3+} while Mn remains dissolved as Mn^{2+} (Figs. 11b and 11c). Therefore, these hardgrounds likely formed under lower pH and/or Eh conditions than those characterizing the Valanginian – Hauterivian (DU1/CP1) event. Notably, the HG3a-b hardgrounds mark the transition to pelagic limestone deposition (Amerillo Fm, *i.e.*, the drowning of the Panormide platform) and, compared to the other hardgrounds, they are the most enriched of CFA (Fig. 7). This suggests elevated phosphorous concentrations at the top of the platform during the Turonian – Campanian likely related to the stage of descent of the platform toward the OMZ (Fig. 11c).

The $\delta^{13}C$ and $\delta^{18}O$ isotopic curves provide further insights into the paleoenvironmental conditions during the three demise events. Notably, both isotopic curves show a sharp shift towards negative values in correspondence of the phosphatized Fe-Mn oxides rich hardgrounds (HGs in Fig. 3). The sharp negative shift of the $\delta^{13}C$ curves (green spheres in Fig. 9) can be related to massive release of isotopically light carbon to the atmosphere/hydrosphere reservoirs from excess venting of volcanogenic CO_2 or methane release from clathrate dissociation (Jahren et al., 2001; Beerling et al., 2002; Milkov, 2004; Mehay et al., 2009). Notably, excess of CO_2 at the time of formation of the HGs can be related to intensive volcanism (Large Igneous Provinces, Fig. 10): Paraná-Etendeka (136-133 Ma), Ontong-Java Plateau-Manihiki Plateau

(125-123 Ma), Kerguelen Plateau-Rajmahal Traps (118 Ma) and Caribbean-Colombian Province (90 Ma) (see Gale et al., 2020). Regarding the $\delta^{18}O$ record (blue spheres in Fig. 9), the negative shifts during the formation of the HGs indicate warm climatic pulses. In detail, the rise in temperature, recorded during the HG1 hardgrounds, was accompanied by reduced storage capacity of ^{13}C-enriched carbonate carbon, increased availability of nutrients, mostly by deep and cool water (*i.e.*, upwelling), despite oxic conditions being present at the sea floor (*e.g.*, Westermann et al., 2010). The latter condition is consistent with the oxidation of both Mn and Fe at the top of the platform (see the schematic model given in Fig. 11a). In the case of the formation of the HG2 hardground the warm and humid climate pulse was accompanied by enhanced weathering, higher runoff and increased detrital input (Fig. 11b; Basilone et al., 2017) resulted in the most intense water stratification and less efficient bottom-water renewal, with the establishment of suboxic conditions (*e.g.*, Gambacorta et al., 2023). These redox (suboxic) conditions triggered the separation between Mn and Fe. The former remains as dissolved Mn^{2+} while the oxidation of Fe produced the fine mixture of goethite and hematite (see the schematic model given in Fig. 11b).

The texture and mineral composition of the HG3 hardgrounds and associated pelagites, characterized by abundant Fe-oxides and CFA (Table 2), are comparable with the onset of the worldwide recorded Upper Cretaceous oceanic red beds (*i.e.*, CORBs, Wagreich and Krenmayr, 2005; Hu et al., 2005; Wang et al., 2011), suggesting an enrichment of phosphorous and nutrients from upwelling (Alvarez et al., 1990; De Carlo, 1991; Baumgartner, 2013).

On the other hand, the sharp positive shift of the $\delta^{18}O$ curves below and above each HGs hardground (CP1, CP2, CP3 and AMM in Fig. 9) reveals that cold climatic conditions fuelled the demise and drowning of the carbonate platform. These events could be correlated with the cooling pulses wide world recorded and considered as icehouse interludes during the Cretaceous greenhouse mode, frequently recorded in correspondence of the environmental stress of the OAEs (Price et al., 2000; Pucéat et al., 2003; McArthur et al., 2007; Cavalheiro et al., 2021).

Conclusions

Detailed stratigraphic study of the Cretaceous Panormide shallow-water limestone of the Colombrina section (Palermo Mts., NW Sicilian fold and thrust belt) allowed recognizing three main drowning unconformities marked by submarine phosphatized Fe-Mn rich hardgrounds and condensed pelagic carbonates. These events occurred in the Valanginian-Hauterivian, upper Aptian-Albian and Turonian-Early Campanian time intervals respectively, marked repeated long-term demise of the carbonate platform. Regional to global correlations highlight similarities, in terms of sedimentological features and time of formation, with the drowning features described both from the Northern and Southern Tethyan Cretaceous shallow-water carbonates and with the excursions of the carbon isotopic cycle in coincidence with the OAEs recorded world-wide in the Cretaceous pelagites (*e.g.*, Weissert, Selli and Bonarelli events).

PXRD, SEM-EDS and RS results suggest that the demise events (HGs) are genetically related to episodic perturbations of the redox conditions at the platform seafloor. The phosphatized HG1 hardgrounds formed during the lowermost demise event consist of Mn and Fe oxides dispersed in a calcite matrix, suggesting oxic conditions. In strong contrast, the other phosphatized hardgrounds (HG2 and HG3) are free of Mn, suggesting suboxic conditions at the platform seafloor during these events.

The isotopic (C and O) curves show sharp negative shift during the formation of the three hardgrounds followed by rapid positive shift indicating that the paleoenvironmental perturbations were influenced by the pCO_2 cycle and by the alternation of icehouse to greenhouse conditions characterizing the Cretaceous climate during the considered intervals.

Our multidisciplinary work suggests that an interplay among synsedimentary tectonics and paleoenvironmental stresses have induced the demise of the carbonate platform, producing the drowning unconformity surfaces and the associated hardgrounds. In this view, the original setting of the Panormide would be seen as a carbonate platform that, subjected to tectonics with tensional-to-compressional regime, evolved in a block dissected platform with morphostructural high and low, where the effects of paleoenvironmental and paleoclimate changes (*i.e.*, mineralisation and condensation) are more easily readable in the stratigraphic column than in other areas not affected by synsedimentary tectonics.

Acknowledgments

The research was supported by grants from CAPES (Coordenação de Aperfeiçoamento de Pessoal de Nivel Superior) “Ciências do Mar II” (resp. Prof. L. Jovane). Funding for research was provided by CARG Project (F_594-585 Partinico-Mondello fondi della Legge 305/89) (resp. Prof. A. Sulli). The Grant to Department of Science, Roma Tre University (MIUR-Italy Dipartimenti di Eccellenza, ARTICOLO 1, COMMI 314-337 LEGGE 232/2016) is gratefully acknowledged. L. M. Nieto: Research Group RNM200 (UJA-Junta de Andalucía) and Research Project 1380715 (FEDER-UJA). GeoLab laboratory (Palermo, Italy) is acknowledged for the initial analyses conducted on the hardground samples

References

Agate, M., Basilone, L., Di Maggio, C., Contino, A., Pierini, S., Catalano, R., 2017. Quaternary marine and continental unconformity-bounded stratigraphic units of the NW Sicily coastal belt. Journal of Maps 13, 425–437.

Aguado, R, Company M, Castro JM, de Gea GA, Molina JM, Nieto LM, Ruiz-Ortiz PA, 2018. A new record of the Weissert episode from the Valanginian succession of Cehegín (Subbetic, SE Spain): bio- and carbon isotope stratigraphy. Cretaceous Research 92, 122–137. https://doi.org/10.1016/j.cretres.2018.07.010

Allemann, F., Catalano, R., Farès, F., Remane, J., 1971. Standard Calpionellid zonation (Upper Tithonian–Valanginian) of the western Mediterranean province. Proc. of the II Planktonic Conference Roma 1970, 1337–1340

Alvarez, R., De Carlo, E. H., Cowen, J., Andermann G., 1990. Micromorphological characteristics of a marine ferromanganese crust. Mar. Geol, 94, 239–249.

Arthur, M.A., Jenkyns, H.C., Brumsack, H.J. & Schlanger, S.O. 1990. Stratigraphy, geochemistry and palaeogeography of organic carbon-rich Cretaceous sequences. In: Ginsburg, R.N. & Beaudoin, B. (eds) Cretaceous Resources, Events and Rhythms. Kluwer, Dordrecht, 75–119.

Basilone, L., 2009. Sequence stratigraphy of a Mesozoic carbonate platform-to-basin system in western Sicily. Central European Journal of Geoscience 1, 251–273.

Basilone, L., 2011. Geological Map of the Rocca Busambra-Corleone region (western Sicily, Italy): explanatory notes. Ital. J. Geosci. (Boll. Soc. Geol. It.) 130, 42–60. DOI: 10.3301/IJG.2010.17

Basilone, L., Di Maggio, C., 2016. Geology of Monte Gallo (Palermo Mts, NW Sicily). Journal of Maps 1–12. doi:10.1080/17445647.2015.1124716

Basilone, L., Sulli, A., 2016. A facies distribution model controlled by a tectonically inherited sea bottom topography in the carbonate rimmed shelf of the Upper Tithonian-Valanginian Southern Tethyan continental margin (NW Sicily, Italy). Sedim. Geol. 342, 91–105. doi:10.1016/j.sedgeo.2016.06.013

Basilone, L., Perri, F., Sulli, A., & Critelli, S., 2017. Paleoclimate and extensional tectonics of short-lived lacustrine environments. Lower Cretaceous of the Panormide Southern Tethyan carbonate platform (NW Sicily). Marine and Petroleum Geology, 88, 428–439. https://doi.org/10.1016/j.marpetgeo.2017.08.041

Basilone, L., Sulli, A., 2018. Basin analysis in the Southern Tethyan margin: Facies sequences, stratal pattern and subsidence history highlight extension-to-inversion processes in the

Cretaceous Panormide carbonate platform (NW Sicily). Sedimentary Geology 363, 235–251. https://doi.org/10.1016/j.sedgeo.2017.11.013

Basilone, L., 2018. Lithostratigraphy of Sicily. Unipa Springer Series. Springer International Publishing AG, Cham (349 pp.).

Basilone, L., 2020. Mesozoic tectono-sedimentary evolution of the Trapanese Southern Tethyan margin (NW Sicily), integrating facies and stratigraphic analysis with subsi- dence history. Italian Journal of Geosciences (Boll. Soc. Geol. It.) 139, 54–75.

Basilone, L., 2021a. Valanginian cold/warm climatic oscillations and synsedimentary tectonics interaction for drowning carbonate platform of Southern Tethys (Sicily). Sedimentary Geology, 423, 105991. https://doi.org/10.1016/j.sedgeo.2021.105991

Basilone, L., 2021b. Synsedimentary tectonics vs paleoclimatic changes across the Aptian–Albian boundary along the Southern Tethyan margin: the Panormide carbonate platform case history (NW Sicily). Marine and Petroleum Geology 124, 104801. https://doi.org/10.1016/j.marpetgeo.2020.104801.

Basilone, L., 2022. Jurassic–cretaceous intraplatform basins from NW Sicily fold and thrust belt: Implications for oblique rifting of the Southern Tethyan margin. Sedimentary Geology, 106255. https://doi.org/https://doi.org/10.1016/j.sedgeo.2022.106255

Baturin, G. N., 1989. The origin of marine phosphorites. International Geology Review, 31(4), 327–342. https://doi.org/10.1080/00206818909465885

Baumgartner, P.O., 2013. Mesozoic radiolarites — accumulation as a function of sea surface fertility on Tethyan margins and in ocean basins. Sedimentology 60, 292–318.

Beerling, D.J., Lomas, M.R., Gröcke, D., 2002. On the nature of methane gas-hydrate dissociation during the Toarcian and Aptian oceanic anoxic events. American Journal of Science 302, 28–49.

Benites, M., Hein, J.R., Mizell, K., Blackburn, T., Jovane, L., 2020. Genesis and evolution of ferromanganese crusts from the summit of Rio Grande rise, Southwest Atlantic Ocean. Minerals 10, 1–36.

Benninger, L., Hein, J.R., 2000. Diagenetic Evolution of Seamount Phosphorite. In: C. R. Glenn, L. Prévôt-Lucas, J. Lucas (Eds), Marine Authigenesis: from Global to Microbial, SEPM, Special Publication, v. 60, https://doi.org/10.2110/pec.00.66.0245

Bernardini, S., Bellatreccia F., Casanova M.A., Della Ventura G., Sodo A., 2019. Raman spectra of natural manganese oxides. Journal of Raman Spectroscopy, 50, 873–888.

Bernardini, S., Bellatreccia, F., Della Ventura, G., Ballirano, P., Sodo, A., 2020. Raman spectroscopy and laser-induced degradation of groutellite and ramsdellite, two cathode materials of technological interest. RSC Advances, 10, 923–929.

Bernardini, S., Bellatreccia, F., Columbu, A., Vaccarelli, I., Pellegrini, M., Jurado, V., Del Gallo, M., Saiz-Jimenez, C., Sodo, A., Millo, C., Jovane, L., De Waele, J., 2021a. Morpho-mineralogical and bio-geochemical description of cave manganese stromatolite-like patinas (Grotta del Cervo, Central Italy) and hints on their paleohydrological-driven genesis. Front. Earth Sci. 9, 765 642667.

Bernardini, S., Bellatreccia, F., Della Ventura, G., and Sodo, A., 2021b. A Reliable Method for Determining the Oxidation State of Manganese at the Microscale in Mn Oxides *via* Raman Spectroscopy. Geostand. Geoanal. Res. 45, 223–244.

Bernardini, S., Della Ventura, G., Sodo, Benites, M., Jovane, L., Hein, J.R., Lucci, F., 2023. Micro-Raman mapping of critical metals (Li, Co, Ni) in a rhythmically laminated deep-ocean ferromanganese deposit. Geochemistry, 126014.

Berner, R.A., 1981. A new geochemical classification of sedimentary environments. J. Sediment. Petrol. 51, 359–365.

Bonardi, G., Cavazza, W., Perrone, V., & Rossi, S. (2001). Calabria-peloritani terrane and Northern Ionian Sea. In G. B. Vai & I. P. Martini (Eds.), Anatomy of an orogen: The Apennines and adjacent Mediterranean basins (pp. 287–306). Dordrecht: Kluwer Academic.

Bosence D.W.J., 2005. A Genetic Classification of Carbonate Platforms Based on Their Basinal and Tectonic Settings in the Cenozoic. Sedimentary Geology 175: 49–72. DOI: 10.1016/j.sedgeo.2004.12.030

Bourrouilh, R., Bourque, P.-A., Dansereau, P., Bourrouilh-Le Jan, F., Weyant, P., 1998. Synsedimentary tectonics, mud-mounds and sea-level changes on a palaeozoic carbonate platform margin: a Devonian Montagne Noire example (France). Sedimentary Geology 118, 95–118.

Brandano, M., Cornacchia, I., Raffi, I., Tomassetti, L., 2016. The Oligocene–Miocene stratigraphic evolution of the Majella carbonate platform (Central Apennines, Italy). Sedimentary geology, 333, 1–14.

Camoin, G., 1983. Plate-formes carbonates et recifs a Rudistes du Cretaceé de Sicile. These de Doctorat n.13, 1-244 (Unpublished doctoral dissertation). Université dé Provence, Marseille.

Carannante, G., Cherchi, A., Graziano, R., Ruberti, D., Simone L., 2008. Post-Turonian rudist-bearing limestones of the peri-Tethyan Region: Evolution of the sedimentary patterns and lithofacies in the context of global vs. regional controls. In: Lukasik J. & Simo A. (eds), Controls on carbonate platform and reef development. SEPM Spec. Publ. 89, 255–270.

Caron, M., 1985. Cretaceous planktic foraminifera. In: Bolli, H.M., Saunders, J.B., Perch-Nielsen, K. (Eds.), Plankton Stratigraphy, vol. 1. Cambridge Univ. Press., pp. 17–86

Catalano R., Di Stefano P., Sulli A. & Vitale F.P., 1996. Paleogeography and structure of the

Central Mediterranean: Sicily and its offshore area. Tectonophysics 260, 291–323.

Catalano, R., Franchino, A., Merlini, S., Sulli, A., 2000. Central western Sicily structural setting interpreted from seismic reflection profiles. Mem. Soc. Geol. It. 55, 5–16

Catalano, R., Valenti, V., Albanese, C., Accaino, F., Sulli, A., Tinivella, U., Gasparo Morticelli, M., Zanolla, C., & Giustiniani, M., 2013a. Sicily's fold-thrust belt and slab roll-back: The SI.RI.PRO. seismic crustal transect. Journal of the Geological Society, 170(3), 451–464. https://doi.org/10.1144/jgs2012-099

Catalano R., Basilone L., Di Maggio C., Gasparo Morticelli M., Agate M., Avellone G., 2013b. Note illustrative della Carta Geologica d'Italia alla scala 1:50.000 del foglio 594-585 "Partinico-Mondello", 271 pp., Progetto Carg, ISPRA-Regione Siciliana.

Catalano, R., Avellone, G., Basilone, L., Sulli, A., 2013c. Note illustrative della Carta Geologica d'Italia alla scala 1:50.000 del Foglio n. 595 "Palermo", 218 pp. Progetto Carg, ISPRA-Regione Siciliana.

Cavalheiro, L., Wagner, T., Steinig, S. et al. Impact of global cooling on Early Cretaceous high pCO_2 world during the Weissert Event. (2021) Nature Communication 12, 5411. https://doi.org/10.1038/s41467-021-25706-0

Channell, J.E.T., Oldow, J., Catalano, R., D'Argenio. B., 1990. Palaeomagnetically Determined Rotations in the Western Sicilian Fold and Thrust Belt. Tectonics, 9 (4), 641–660.

Charbonnier, G., Boulila, S., Gardin, S., Duchamp-Alphonse, S., Adatte, T., Spangenberg, J. E., Föllmi, K. B., Colin, C., Galbrun, B., 2013. Astronomical calibration of the Valanginian "Weissert" episode: The Orpierre marl-limestone succession (Vocontian Basin, southeastern France). *Cretaceous Research*, *45*, 25–42.

Chatalov, A., Bonev, N., Ivanova, D., 2015. Depositional characteristics and constraints on the mid-Valanginian demise of a carbonate platform in the intra-Tethyan domain, Circum-Rhodope Belt, northern Greece. Cretaceous Research 55, 84–115.

Chiarabba, C., De Gori, P., Speranza, F., 2008. The southern Tyrrhenian subduction zone: Deep geometry, magmatism and Plio- Pleistocene evolution. Earth Planet. Sci. Lett., 268, 408-423;

Chiocchini M., Chiocchini, R.A., Didaskalou, P., Potetti, M. (2008). Upper Triassic, Jurassic and Cretaceous microbiostratigraphy of the carbonatic platform facies in the central-southern Latium and Abruzzi. In: Chiocchini, M. (Ed.), Micropaleontological and Biostratigraphical Researches on the Mesozoic of the Latium-Abruzzi Carbonate Platform (Central Italy). Memorie Descrittive della Carta Geologica d'Italia, 84, 1-169.

Clari PA, Dela Pierre F, Martire L (1995) Discontinuities in carbonate successions: identification, interpretation and classification of some Italian examples. Sediment Geol 100, 97–121

Cohen, K.M., Finney, S.C., Gibbard, P.L., Fan, J.-X., 2013. The ICS international chronostratigraphic chart. Episodes 36, 199–204.

Cronan DS, Galacz A, Mindszenty A, Moorby SA, Polgari M. 1991. Tethyan ferromanganese oxide deposits from Jurassic rocks in Hungary. Journal of the Geological Society, London 148: 655–668.

Danisch J, Krencker FN, Mau M, Mattioli E, Faure P, Almeras Y, Nutz A, Kabiri L, El Ouali M, Bodin S (2021) Tracking a drowning unconformity up to the peritidal zone: Proximal expression of the early Bajocian carbonate crisis in Morocco. Journal of African Earth Sciences 182:104300. DOI 0.1016/j.jafrearsci.2021.104300

De Carlo, E.H., 1991. Paleoceanographic implications of rare earth element variability within a Fe–Mn crust from the central Pacific Ocean. Marine Geology 98, 449–467.

De Castro, P., 1991. Mesozoic. In: Barattolo, F., De Castro, P., Parente, M. (Eds.). V Int. Symp. Fossil. Algae, Field trip Guide Book, pp. 21-38.

Di Maggio, C., Agate, M., Contino, A., Basilone, L., Catalano, R., 2009. Unconformity-bounded stratigraphic units of Quaternary deposits mapped for the CARG Project in Northern and Western Sicily [Unità a limiti inconformi utilizzate per la cartografia dei depositi quaternari nei fogli CARG della Sicilia nord-occidentale]. Alpine and Mediterranean Quaternary 22 (2), 345–364 (Open Access).

Di Maggio, C., Madonia, G., Vattano, M., Agnesi, V., Monteleone, S., 2017. Geomorphological evolution of western Sicily, Italy. Geol. Carpathica 68, 80–93. https://doi.org/10.1515/geoca-2017-0007

Di Stefano, P., Ruberti, D., 2000. Cenomanian Rudist-dominated shelf-margin limestones from the Panormide Carbonate Platform (Sicily, Italy): facies analysis and sequence stratigraphy. Facies 42, 133–160.

Dromart, G., Garcia, J.-P., Gaumet, F., Picard, S., Rousseau, M., Atrops, F., Lécuyer, C., Shepard, S.M.F. (2003) Perturbation of the carbon cycle at the Middle/Late Jurassic transition: geological and geochemical evidence. American Journal of Science 303, 667–707.

Dunham, R.J., 1962. Classification of carbonate rocks according to depositional textures. In: Ham, W.E. (Ed.), Classification of Carbonate Rocks. American Association of Petroleum Geologists Memoir. 1: 108–121.

Finetti, I.R., 2005. Geodynamic evolution of the Mediterranean region from the Permo–Triassic Ionian opening to the present, constrained by new lithospheric CROP seismic data. In: Finetti, I.R. (Ed.), CROP PROJECT, Deep Seismic Exploration of the Central

Mediterranean and Italy. Atlas in Geoscience, 1. Elsevier, pp. 767–776.

Föllmi, K.B., Weissert, H., Bisping, M., Funk, H., 1994. Phosphogenesis, carbon isotope stratigraphy and carbonate platform evolution along the Lower Cretaceous northern Tethyan margin. Geological Society of America Bulletin 106, 729–746.

Föllmi, K.B., Gainon, F., 2008. Demise of the northern Tethyan Urgonian carbonate platform and subsequent transition towards pelagic conditions: the sedimentary record of the Col de la Plaine Morte area, central Switzerland. Sedimentary Geology, 205, 142-159.

Föllmi, K.B., Godet A. 2013. Palaeoceanography of Lower Cretaceous Alpine platform carbonates. Weissert H (ed). Sedimentology **60**: 131–151. DOI: 10.1111/sed.12004

Gale AS, Mutterlose J, Batenburg S, Gradstein FM, Agterberg FP, Ogg JG, Petrizzo MR (2020) The Cretaceous Period. In: Gradstein FM, Ogg JG, Schmitz MD, Ogg GM (eds) Geologic Time Scale, vol 2. Elsevier, Amsterdam, pp 1023–1086.

Gambacorta, G., Cavalheiro, L., Brumsack, H.J., Dickson, A.J., Jenkyns, H.C., Schnetger, B., Wagner, T., Erba, E., 2023. Suboxic conditions during the Toarcian Oceanic Anoxic Event in the Alpine-Mediterranean Tethys: the Sogno Core pelagic record (Lombardy Basin, northern Italy). Glob. Planet. Chang. 104089

Gasparo Morticelli, M., Valenti, V., Catalano, R., Sulli, A., Agate, M., Avellone, G., Albanese, C., Basilone, L., Gugliotta, C., 2015. Deep controls on foreland basin system evolution along the Sicilian fold and thrust belt. Bulletin de la Societé géologique de France 186, 273–290.

Godet, A., 2013. Drowning unconformities: Palaeoenvironmental significance and involvement of global processes. Sedim. Geol. 293, 45–66. doi 10.1016/j.sedgeo.2013.05.002

Gonzalez, F.J., Somoza, L., Leon, R., Medialdea, T., Torres, T., Ortiz, J.E., Lunar, R., Martínez-Frías, J., Merinero, R., 2012. Ferromanganese nodules and micro-hardgrounds associated with the Cadiz Contourite Channel (NE Atlantic): palaeoenvironmental records of fluid venting and bottom currents. Chem. Geol. 310-311, 56–78.

Grădinaru, M., Lazar, I., Bucur, I.I., Grădinaru, E., Săsăran, E., Ducea, M.N., Andrăşanu, A., 2016. The Valanginian history of the eastern part of the Getic carbonate platform (Southern Carpathians, Romania): evidence for emergence and drowning of the platform. Cretaceous Research 66, 11–42.

Graziano R. 2013. Sedimentology, biostratigraphy and event stratigraphy of the Early Aptian Oceanic Anoxic Event (OAE1A) in the Apulia Carbonate Platform Margin - Ionian Basin System (Gargano Promontory, southern Italy). Cretaceous Research 39, 78–111.

Haq BU, Hardenbol J, Vail PR. 1987. Chronology of Fluctuating Sea Levels since the Triassic. Science 235, 1156–1167. DOI: 10.1126/science.235.4793.1156

Hein, J.R., Koschinsky, A., Bau, M., Manheim, F.T., Kang, J.K., Roberts, L., 2000. Cobalt rich ferromanganese crusts in the Pacific. In: Cronan, D.S. (Ed.), Handbook of Marine Mineral Deposits. CRC Press, Boca Raton, Florida, pp. 239–279.

Hein, J.R., Koschinsky, A., 2014. Deep-Ocean Ferromanganese Crusts and Nodules. In: Holland, H.D., Turekian, K.K. (Ed.), Treatise on Geochemistry. Elsevier, 13, 273–291 ().

Hem, J.D., 1963. Chemical equilibria affecting the behaviour of manganese in natural water. Hydrological Sciences Journal, 8, 30–37.

Hem, J.D., 1972. Chemical factors that influence the availability of iron and manganese in aqueous systems. Geol. Soc. Am. Bull. 83, 443–450.

Henriquet, M., Dominguez, S., Barreca, G., Malavieille, J., Monaco, C., 2020. Structural and tectono-stratigraphic review of the Sicilian orogen and new insights from analogue modeling. Earth-Science Reviews 208, 103257. https://doi.org/10.1016/j.earscirev.2020.103257.

Hu, X., Jansa, L., Wang, C., Sarti, M., Bak, K., Wagreich, M., Michalík, J., Sotak, J., 2005. Upper Cretaceous oceanic red beds (CORBs) in the Tethys: occurrences, lithofacies, age, and environments. Cretaceous Research 26, 3–20. doi:10.1016/j.cretres.2004.11.011

Huck, S., Heimhofer, U., Immenhauser, A., Weissert, H., 2013. Carbon-isotope stratigraphy of Early Cretaceous (Urgonian) shoal-water deposits: Diachronous changes in carbonate-platform production in the north-western Tethys. Sedim. Geol. 290, 157–174. doi:10.1016/j.sedgeo.2013.03.016

Husinec, A., Sokač, B., 2006. Early Cretaceous benthic associations (foraminifera and calcareous algae) of a shallow tropical-water platform environment (Mljet Island, southern Croatia). Cretaceous Research 27, 418–441.

Immenhauser, A., Hillgartner, H., Van Bentum, E., 2005. Microbial-foraminiferal episodes in the Early Aptian of the southern Tethyan margin: ecological significance and possible relation to oceanic anoxic event 1a. Sedimentology 52, 77-99.

Jahren, A.H., Arens, N.C., Sarmiento, G., Guerrero, J., Amundson, R., 2001. Terrestrial record of methane hydrate dissociation in the Early Cretaceous. Geology 29, 159–162.

James, N.P., Choquette, P.W., 1983. Diagenesis 6. Limestones — The Sea Floor Diagenetic Environment. Geoscience Canada 10.

Jenkyns HC (1970) Growth and disintegration of carbonate platform. N Jb Geol Paläont Mh 6:325–344

Jenkyns, H. C., 2018. Transient cooling episodes during Cretaceous Oceanic Anoxic Events with special reference to OAE 1a (Early Aptian). Philosophical Transactions of the Royal Society A: 376 (2130). https://doi.org/10.1098/rsta.2017.0073

Jenkyns, H.C., Wilson, P.A., 1999. Stratigraphy, paleoceanography, and evolution of Cretaceous Pacific guyots: relics from a greenhouse Earth. American Journal of Science 299, 341-392.

Kfouri, L.O., Millo, C., de Lima, A.E., Semiramis Silveira, C., Gomes Sant'Anna, L., Marino, E., González, F.J., Jamil Sayeg, I., Hein, J.R., Jovane, L., Bernardini, S., Lusty, P.A.J., Murton, B.J., 2021. Growth of ferromanganese crusts on bioturbated soft substrate, Tropic Seamount, northeast Atlantic Ocean. Deep Sea Res., Part I 175, 103586 (2021).

Kleypas, J.A., Buddemeier, R.W., Archer, D., Gattuso, J.P., Langdon, C., Opdyke, B.N., 1999. Geochemical consequences of increased atmospheric carbon dioxide on coral reefs. Science 284, 118-120.

Koschinsky, A., Halbach, P., Hein, J.R., Mangini, A., 1996. Ferromanganese crusts as indicators for paleoceanographic events in the NE Atlantic. Geologische Rundschau 85, 567–576.

Koschinsky, A., Hein, J.R. 2017. Marine Ferromanganese Encrustations: Archives of Changing Oceans. Elements 13, 177–182.

Kraal, P., Slomp, C.P., Reed, D.C., Reichart, G.J., Poulton, S.W., 2012. Sedimentary phosphorus and iron cycling in and below the oxygen minimum zone of the northern Arabian Sea. Biogeosciences, 9, 2603–2624

Larson, R.L., Erba, E., 1999. Onset of the mid-Cretaceous greenhouse in the Barremian-Aptian: igneous events and the biological, sedimentary, and geochemical responses. Paleoceanography 14, 663–678.

Lees, A., Buller, A.T., 1972. Modern temperate water and warm water shelf carbonate sediments contrasted. Marine Geology 13, 1767-1773.

Lukeneder, A., Sotak, J., Jovane, L., Giorgioni, M., Savian, J.F., Halásová, E., Reháková, D., Józsa, Š., Kroh, A., Florindo, F., Sprovieri, M., 2016. Multistratigraphic records of the Lower Cretaceous (Valanginian–Cenomanian) Puez key area in N. Italy. Palaeogeography 447, 65–87.

Mallarino G., Goldstein R. H., Di Stefano P., 2002. New approach for quantifying water depth applied to the enigma of drowning of carbonate platforms. Geology, 30 (9): 783–786

Maynard J.B., 2010. The chemistry of manganese ores through time: A signal of increasing diversity of Earth-surface environments. Economic Geology, 105, 535–552.

McArthur, J.M., Janssen, N.M.M., Reboulet, S., Leng, M.J., Thirlwall, M.F., van de Schootbrugge, B., 2007. Palaeo-temperatures, polar ice-volume, and isotope stratigraphy (Mg/Ca, $\delta^{18}O$, $\delta^{13}C$, $^{87}Sr/^{86}Sr$): the Early Cretaceous (Berriasian, Valanginian, Hauterivian). Palaeogeography, Palaeoclimatology, Palaeoecology 202, 252–272.

Mehay, S., Keller, C.E., Bernasconi, S.M., Weissert, H., Erba, E., Bottini, C., Hochuli, P.A., 2009. A volcanic CO_2 pulse triggered the Cretaceous Oceanic Anoxic Event 1a and a biocalcification crisis. Geology 37, 819-822.

Menegatti, A.P., Weissert, H., Brown, R.S., Tyson, R.V., Farrimond, P., Strasser, A., Caron, M., 1998. High-resolution $\delta^{13}C$ stratigraphy through the early Aptian “Livello Selli” of the Alpine Tethys. Paleoceanography 13, 530-545.

Milkov, A.V., 2004. Global estimates of hydrate-bound gas in marine sediments: how much is really out there? Earth-Science Reviews 66, 183–197.

Mills, R. A., Wells, D. M., Roberts, S., 2001. Genesis of ferromanganese crusts from the TAG hydrothermal field. Chemical geology, 176(1-4), 283–293.

Mindszenty, A., D’Argenio, B., Aiello, G. 1995. Lithospheric bulges recorded by regional unconformities. The case of Mesozoic–Tertiary Apulia. Tectonophysics 252, 137–161.

Montanari L., 1965. Geologia del Monte Pellegrino (Palermo). Riv. Min. Sic., 15, 1–64.

Mutti, M., Bernoulli, D., 2003. Early Marine Lithification and Hardground Development on A Miocene Ramp (Maiella, Italy): Key Surfaces to Track Changes in Trophic Resources in Nontropical Carbonate Settings. Journal of Sedimentary Research, 73, 296–308.

Nieto LM, Rodríguez-Tovar FJ, Molina JM, Reolid M, Ruiz-Ortiz PA., 2014. Unconformity surfaces in pelagic carbonate environments: a case from the middle Bathonian of the Betic Cordillera, SE Spain. Annales Societatis Geologorum Poloniae 84, 281–295.

Orr, J.C., Fabry, V.J., Aumont, O., Bopp, L., Doney, S.C., Feely, R.A., Gnanadesikan, A., Gruber, N., Ashida, A., Joos, F., Key, R.M., Lindsay, K., Maier-Reimer, E., Matear, R., Monfray, P., Mouchet, A., Najjar, R.G., Plattner, G.K., Rodgers, K.B., Sabine, C.L., Sarmiento, J.L., Schlitzer, R., Slater, R.D., Totterdell, I.J., Weirig, M.F., Yamanaka, Y., Yool, A., 2005. Anthropogenic ocean acidification over the twenty-first century and its impact on calcifying organisms. Nature 437, 681-686.

Parente M., Frijia G., Di Lucia M., 2007. Carbon-isotope stratigraphy of Cenomanian-Turonian platform carbonates from the southern Appennines (Italy): a chemostratigraphic approach to the problem of correlation between shallow water and deep-water successions. Journal of the Geol. Soc., London 164, 609–620.

Paytan, A., McLaughlin, K., 2007. The Oceanic Phosphorus Cycle. Chem. Rev., 107, 563−576.

Peter, A.D., Simo, T., 1997. Carbonate platform drowning and oceanic anoxic events on a Mid-Cretaceous carbonate platform, south-central Pyrenees, Spain. Journal of Sedimentary Research 67, 698–714.

Pomar, L., 2020. Carbonate systems. In: Regional Geology and Tectonics, Scarselli N, Adam J, Chiarella D, Roberts DG, Bally AW (eds), Elsevier, Oxford, pp. 235–311.

Price, G.D., Ruffell, A.H., Jones, C.E., Kalin, R.M., Mutterlose, J., 2000. Isotopic evidence for temperature variation during the early Cretaceous (late Ryazanian–mid-Hauterivian). Journal of the Geological Society, London 157, 335–343.

Pucéat, E., Lécuyer, C., Sheppard, S.M.F., Dromart, G., Reboulet, S., Grandjean, P., 2003. Thermal evolution of Cretaceous Tethyan marine waters inferred from oxygen isotope composition of fish tooth enamels. Paleoceanography 18. https://doi.org/ 10.1029/2002PA000823. PA1029.

Remane, J., 1998. Les calpionelles; possibilité biostratigraphiques et limitations paléobiogéographiques. Bulletin de la Société Géologique de France 169, 829–839.

Reolid, M., Abad, I., 2019. The Middle-Upper Jurassic unconformity in the South Iberian Palaeomargin (Western Tethys): a history of carbonate platform fragmentation, emersion and subsequent drowning. Journal of Iberian Geology 45, 87–110. 10.1007/s41513-018-0085-z

Santantonio, M., 1993. Facies associations and evolution of pelagic carbonate platform/ basin systems: examples from the Italian Jurassic. Sedimentology 40, 1039–1067.

Schlager, W., 1981. The paradox of drowned reefs and carbonate platforms. GSA Bull. 92, 197–211.

Schlager, W., 2005. Carbonate sedimentology and sequence stratigraphy. Concepts in Sedimentology and Paleontology, 8. SEPM Tulsa, Oklahoma. 200 pp.

Segl, M., Mangini, A., Bonani, G., Hofmann, G., Nessi, M., Suter, M., Wölfi, W., Friedrich, G., Plüger, W., Wiechowski, A., Beer, J., 1984. ^{10}Be dating of a manganese crust from central North Pacific and implications for ocean paleocirculation. Nature 309:540–543.

Servizio Geologico d'’Italia, 2011a. Official geological map of Italy at 1:50.000 scale, sheet 594–585 “Partinico-Mondello”. ISPRA https://www.isprambiente.gov.it/Media/carg/585_594_MONDELLO_PARTINICO/Foglio.html.

Servizio Geologico d'’Italia, 2011b. Official geological map of Italy at 1:50.000 scale, sheet 595 “Palermo”. ISPRA https://www.isprambiente.gov.it/Media/carg/595_PALERMO/Foglio.html.

Simo, J.A., Scott, R.W., Masse, J.P., 1993. Cretaceous carbonate platform: an overview. In: Simo, T. (Ed.), Cretaceous Carbonate Platform. AAPG Mem. 56, 1–14.

Sulli, A., Gasparo Morticelli, M., Agate, M., Zizzo, E., 2021. Active North-Vergent Thrusting in the Northern Sicily Continental Margin in the Frame of the Quaternary Evolution of the Sicilian Collisional System. Tectonophysics 802, 228717.

Sutherland, K.M., Wankel, S.D., Hein, J.R., Hansel, C.M., 2020. Spectroscopic insights into ferromanganese crust formation and diagenesis. Geochem. Geophys. Geosyst. 21, e2020GC009074

Tarduno, J.A., Sliter, W.V., Kroenke, L., Leckie, M., Mayer, H., Mahoney, J.J., Musgrave, R., Storey, M., Winterer, E.L., 1991. Rapid formation of Ontong-Java Plateau by Aptian mantle plume volcanism. Science 254, 399–403.

Tejada, M.L.G., Suzuki, K., Kuroda, J., Coccioni, R., Mahoney, J.J., Ohkouchi, N., Sakamoto, T., Tatsumi, Y., 2009. Ontong Java Plateau eruption as a trigger for the early Aptian oceanic anoxic event. Geol 37, 855–858. doi:10.1130/G25763A.1

Van de Schootbrugge, B., O. Kuhn, T. Adatte, P. Steinmann, and K. B. Föllmi, 2003, Decoupling of P- and Corg-burial following Early Cretaceous (Valanginian–Hauterivian) platform drowning along the NW Tethyan margin: Palaeogeography, Palaeoclimatology, Palaeoecology, 199 (3-4) 315–331. doi:10.1016/S0031-0182(03)00540-6.

Velić,I., 2007. Stratigraphy and palaeobiogeography of Mesozoic benthic foraminifera of the Karst Dinarides (SE Europe). Geologica Croatica 60, 1–60.

Vogt, P.R., 1989. Volcanogenic upwelling of anoxic water - a possible factor in carbonate bank/reef demise and benthic faunal extinctions? GSA Bull. 101, 1225–1245.

Vörös, A. 2012. Episodic sedimentation on a peri-Tethyan ridge through the Middle–Late Jurassic transition (Villány Mountains, southern Hungary). Facies 58, 415–443. DOI: 10.1007/s10347-011-0287-8

Wagreich, M., Krenmayr, H.G., 2005. Upper Cretaceous oceanic red beds (CORB) in the Northern Calcareous Alps (Nierental Formation, Austria): slope topography and clastic input as primary controlling factors. Cretaceous Research 26, 57–64. doi:10.1016/j.cretres.2004.11.012

Wang, C., Hu, X., Huang, Y., Wagreich, M., Scott, R., Hay, W. 2011. Cretaceous oceanic red beds as possible consequence of oceanic anoxic events. Sedim. Geol. 235, 27–37. doi:10.1016/j.sedgeo.2010.06.025

Weissert H, Erba E. 2004. Volcanism, CO_2 and palaeoclimate: a Late Jurassic-Early Cretaceous carbon and oxygen isotope record. Journal of the Geological Society, London 161, 695–702. DOI: 10.1144/0016-764903-087

Weissert, H., Lini, A., Föllmi, K.B., Kuhn, O., 1998. Correlation of Early Cretaceous carbon isotope stratigraphy and platform drowning events: a possible link? Palaeogeography, Palaeoclimatology, Palaeoecology 137, 189-203.

Wen, X., De Carlo, E. H., & Li, Y. H. (1997). Interelement relationships in ferromanganese crusts from the central Pacific ocean: Their implications for crust genesis. Marine Geology, 136(3), 277–297. https://doi.org/https://doi.org/10.1016/S0025-3227(96)00064-3

Wendt, J., 2017. A unique fossil record from neptunian sills: the world's most extreme example of stratigraphic condensation (Jurassic, western Sicily). Acta Geol. Pol. 67, 163–199. https://doi.org/10.1515/agp-2017-0015.

Westermann, S., Follmi, K.B., Adatte, T., Matera, V., Schnyder, J., Fleitmann, D., Fiet, N., Ploch, I., Duchamp-Alphonse, S., 2010. The Valanginian d13C excursion may not be an expression of a global oceanic anoxic event. Earth and Planetary Science Letters 290 (2010), 118–131.

Westermann, S., Duchamp-Alphonse, S., Fiet, N., Fleitmann, D., Matera, V., Adatte, T., Follmi, K.B., 2013. Paleoenvironmental changes during the Valanginian: new insights from variations in phosphorus contents and bulk- and clay mineralogies in the western Tethys. Palaeo 392, 196–208. https://doi.org/10.1016/j. palaeo.2013.09.017.

Wissler, L., Funk, H., Weissert, H., 2003. Response of Early Cretaceous carbonate platforms to changes in atmospheric carbon dioxide levels. Palaeogeography, Palaeoclimatology, Palaeoecology 200, 187-205.

Zarcone G., Di Stefano P. (2010) Mesozoic discontinuities in the Panormide Carbonate Platform: constraints on the palaeogeography of the central Mediterranean. Italian Journal Geoscience, 129, 191–194.

Figure captions

Fig. 1. a) Geologic map of the Palermo Mountains and location of the study area (after Servizio Geologico d'Italia, 2011a, 2011b); inset, tectonic map of central Mediterranean area (after Catalano et al., 2013a); b) simplified geological cross-section showing the ramp and flat geometry of the Panormide tectonic units with the interposition of the Numidian flysch deposits; c) Upper Triassic–Eocene lithostratigraphy of the Panormide succession outcropping in the Palermo Mountains (after Basilone, 2018).

Fig. 2. Cretaceous biostratigraphy of carbonate platform and deep-water deposits of central–southern Tethyan, constraining the lithostratigraphic units of the Panormide outcropping in the Palermo Mountains.

Fig. 3. Synthetic stratigraphic Colombrina section. Each one of the condensed sections (CSs) is draught to more detail, highlighting hardground levels (HGs) and condensed pelagic horizons (CPs).

Fig. 4. a) Detailed view of the lowermost condensed section (CS1 in Fig. 3) and relative unconformity (DU1 in Fig.3). The massive reddish HG1a hardground rests with laterally thinning above the Upper Tithonian-Berriasian Gastropod Limestone (GAS). The brick-red to blackish laminated HG1b hardground is interlayered in the thick condensed pelagites (CP1 in Fig. 3). The latter consists of: i) thin grey bioclastic grainstone-to-packstone (layer a) that rests above the HG1a and onlap the GAS; ii) massive red and grey lumachella wackestone (layers b and c), onlapping the shallow-water limestone (GAS); iii) grey pelagic mudstone and planar laminated to graded packstone-grainstone intercalations with reworked shallow-water fragments (layer d); iv) planar, oblique and

cross-laminated grey and whitish wackestone-packstone (layer e); v) brown-to-yellow phosphatized packstone with thin-shelled bivalve fragments (layer f). Follow upward the Barremian-Lower Aptian Requienid Limestone (REQ); b) vertical to bed-parallel (stratabound) neptunian dykes, cutting the uppermost beds of the Gastropod Limestone (GAS) and filled by mineralized material; c) intermediate condensed section (CS2 in Fig. 3). The unconformity surface (DU2 in Fig. 3), cutting the Barremian-lower Aptian Requienid limestone (REQ), is marked by the HG2 hardground and condensed pelagites (CP2); follow upward the Rudistid limestone (RUD); d) dissolution cavities, occurring in the topmost beds of the REQ, filled by reddish pelagites and occluded by whitish calcite cements, highlighting geopetal structures; e) uppermost condensed section (CS3 in Fig. 3); it consists of a thin hardground (HG3a), marking the unconformity surface (DU3 in Fig. 3) at the top of the Rudistid limestone (RUD), a package of condensed pelagites (CP3), and by another hardground (HG3b) followed upward by the Upper Cretaceous-Paleogene pelagites of the Amerillo Fm (AMM); f) detailed view of the HG3a hardground locally characterized by lamination (arrows).

Fig. 5. Microfacies of the HGs hardgrounds and condensed pelagites (scale bar 1 mm for all images): a) red pelagites consisting of packstone and wackestone with thick-shelled molluscs, intraclasts, crinoids, echinoids (layer a in Fig. 4a); b) red wackestone with *Protopeneroplis* sp., *Calpionellites darderi*, recrystallized radiolarians, mollusc fragments and intraclasts (layer b in Fig. 4a) passing to gray wackestone (layer c in Fig. 4a) through a stylolite surface impregnated by darkish Fe-Mn oxides; c) aligned thin-shelled molluscs, d) uppermost unconformity surface (DU3 in Fig. 3) represented by an irregular dissolution surface cutting the Rudistid limestone (RUD) and covered by the HG3a hardground. The reddish mineralized material impregnates the top of the RUD; e) darkish Fe-Mn oxides filling cavities and stylolites in the hardground layers; f) planar and

oblique laminated condensed pelagites covering the phosphatized HG3a hardground, through a strongly mineralized stylolite surface.

Fig. 6. EDS mapping of Mn and Fe (highly redox-sensitive metals) collected from HG2 and HG3 hardgrounds (A) and from the HG1 hardground (B). Single point EDS spectrum collected from a Mn-rich grain in the HG1 showing the occurrence of Co, Ni, and Cu (C). Fe (red) have been identified in all the HGs while Mn (yellow) occurs only in the HG1 hardground.

Fig. 7. PXRD patterns of the HGs hardgrounds from the Colombrina section. Ca: calcite, Gt: goethite, CFA: carbonate fluoro-apatite.

Fig. 8. Raman spectra collected from the HGs hardgrounds. S1: hematite, S2: goethite, S3: birnessite and/or vernadite. Raman spectra of Fe oxides (S1 and S2) have been collected from all the HGs while that of Mn oxides (birnessite/vernadite) only from the Mn-rich HG1 hardgrounds (see Table 2). The peaks of Mn^{3+} (red) and Mn^{4+} (blue) in the spectrum S3 are assigned according to Bernardini et al. (2021).

Fig. 9. Evolution of the stable isotope compositions ($\delta^{13}C$ and $\delta^{18}O$) along the condensed sections (CSs). Note the sharp negative shifts of both $\delta^{13}C$ and $\delta^{18}O$ during the formation of the HGs hardgrounds.

Fig. 10. Synthetic correlation of the stratigraphic features of the study Cretaceous Panormide carbonate platform, sampled at Colombrina section, with the main oceanographic and stratigraphic events recorded in the Tethyan realm. Main stratigraphic events in the Panormide carbonate platforms: 1. formation labels (GAS: Gastropod Limestone, REQ:

Requienid Limestone, RUD: Rudistid Limestone, AMM: Amerillo Fm) and interlayered condensed section (CS1-3); 2. columnar section with indication of the different Fe-Mn hardgrounds considered in this study (HG1-3) and condensed pelagites (CP1-3); 3. Drowning unconformities (DU1-3) and stratigraphic relationships; 4. Depositional environments and geometric-types of carbonate platforms and redox conditions of the condensed sections; 5. skeletal grain associations; 6. main biota; 7. Major Transgressive (T)/Regressive (R) tectono-eustatic cycles of the Sicilian carbonate platform-basin system (after Basilone, 2009). Main stratigraphic events in the Tethyan carbonate platforms: 1. Main growth crises of the Tethyan carbonate platforms (after Simo et al., 1993); 2. Positives spikes of stable carbon isotopic curve (after Weissert and Erba, 2004); 3. Episodes of enhanced greenhouse condition (after Weissert et al., 1998); 4. Phosphorous accumulation rates (after Föllmi et al., 1994; Föllmi and Godet, 2013); 5. Phases of phosphogenesis, condensation and platform drowning in the Alpine carbonate platforms (after Föllmi and Godet, 2013); 6. Drowning unconformity (blue bold line) and uplift/bauxites sedimentation events (red triangle) in the Apulia and Southern Appennines carbonate platforms (after Mindszenty et al., 1995; Carannante et al., 2008). OAEs. Oceanic anoxic events (after Arthur et al., 1990). LIPs: Large Igneous Provinces, volcanic activity rates of the Paranà province (a, after Stewart et al., 1996), Ontong-Java Plateau1 (b), Ontog Java2 and Carribean Plateau (c, after Tarduno et al., 1991; Tejada et al., 2009). Long- and short-term sea-level curve (Haq et al., 1987).

Fig. 11. Schematic redox models showing the formation of the phosphatized HGs hardgrounds during the repetitive demise (HG1 and HG2) and drowning (HG3) of the Panormide carbonate platform (Colombrina section). The metals typically enriched during hydrogenetic (Co) and diagenetic (Cu and Ni) growth are indicated. Phosphogenesis fuelled by upwelling of nutrients-rich water masses from the OMZ and/or riverine influx

(A and B) or by the drowning of the platform (C) is accompanied by oxidation of Fe^{2+} to Fe^{3+} (*i.e.*, precipitation of goethite, hematite, and magnetite: red arrows) and of Mn^{2+} to $Mn^{3+/4+}$ (*i.e.*, precipitation of birnessite/vernadite: purple arrows) depending on the redox conditions at the seawater-sediment interface. OMZ: oxygen minimum zone (the source of reactive phosphorous (P) and metals).

Table. 1. Facies and lithostratigraphic characteristics of the studied shallow-water carbonates.

Table 2. Sample description and summary of the minerals identified in the HGs hardgrounds integrating OM, SEM-EDS, PXRD, and RS results. Ca: calcite, CFA: carbonate fluoro-apatite, Gt: goethite, He: hematite, Bi/Ve: birnessite and/or vernadite.

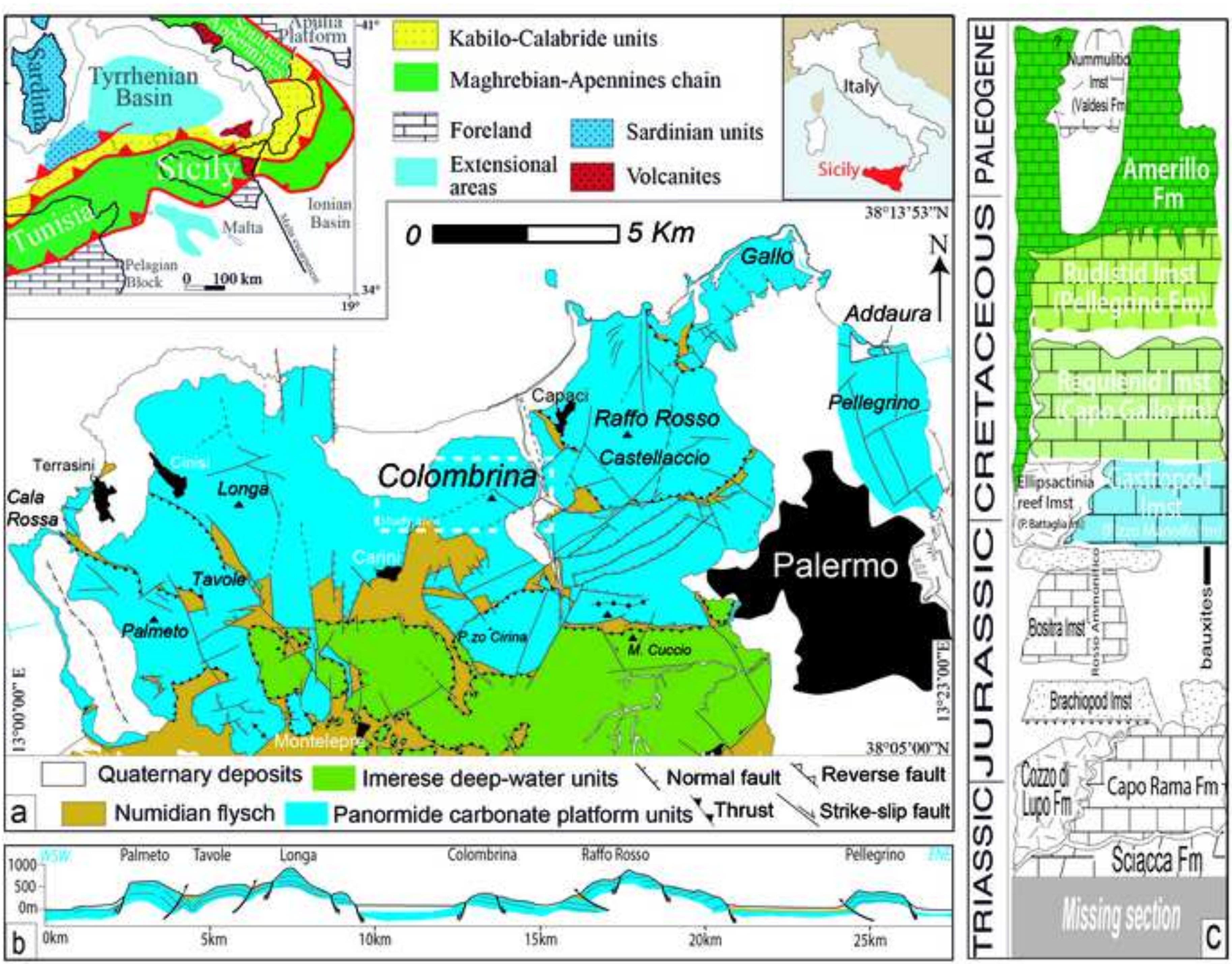
Kabilo-Calabride units
Maghrebian-Apennines chain
Foreland
Sardinian units
Extensional areas
Volcanites
Tyrrhenian Basin
Sardinia
Sicily
Tunisia
Malta
Ionian Basin
Pelagian Block
Apulia Platform
0 100 km
Italy
Sicily
0 5 Km
38°13'53"N
38°05'00"N
13°00'00" E
13°23'00"E
Gallo
Addaura
Pellegrino
Capaci
Raffo Rosso
Castellaccio
Colombrina
Terrasini
Cala Rossa
Longa
Tavole
Palmeto
Carini
P.zo Cirina
M. Cuccio
Montelepre
Palermo
Quaternary deposits
Imerese deep-water units
Normal fault
Reverse fault
Numidian flysch
Panormide carbonate platform units
Thrust
Strike-slip fault
a
WSW
ENE
Palmeto
Tavole
Longa
Colombrina
Raffo Rosso
Pellegrino
1000
500
0m
0km
5km
10km
15km
20km
25km
b
PALEOGENE
CRETACEOUS
JURASSIC
TRIASSIC
Nummulitic lmst (Valdesi Fm)
Amerillo Fm
Rudistid lmst (Pellegrino Fm)
Requienid lmst (Capo Gallo Fm)
Ellipsactinia reef lmst (P. Battaglia Fm)
Gastropod lmst
Bositra lmst
Rosso Ammonitico
bauxites
Brachiopod lmst
Cozzo di Lupo Fm
Capo Rama Fm
Sciacca Fm
Missing section
c

Figure 2

Click here to access/download;Figure;Fig. 2.tif

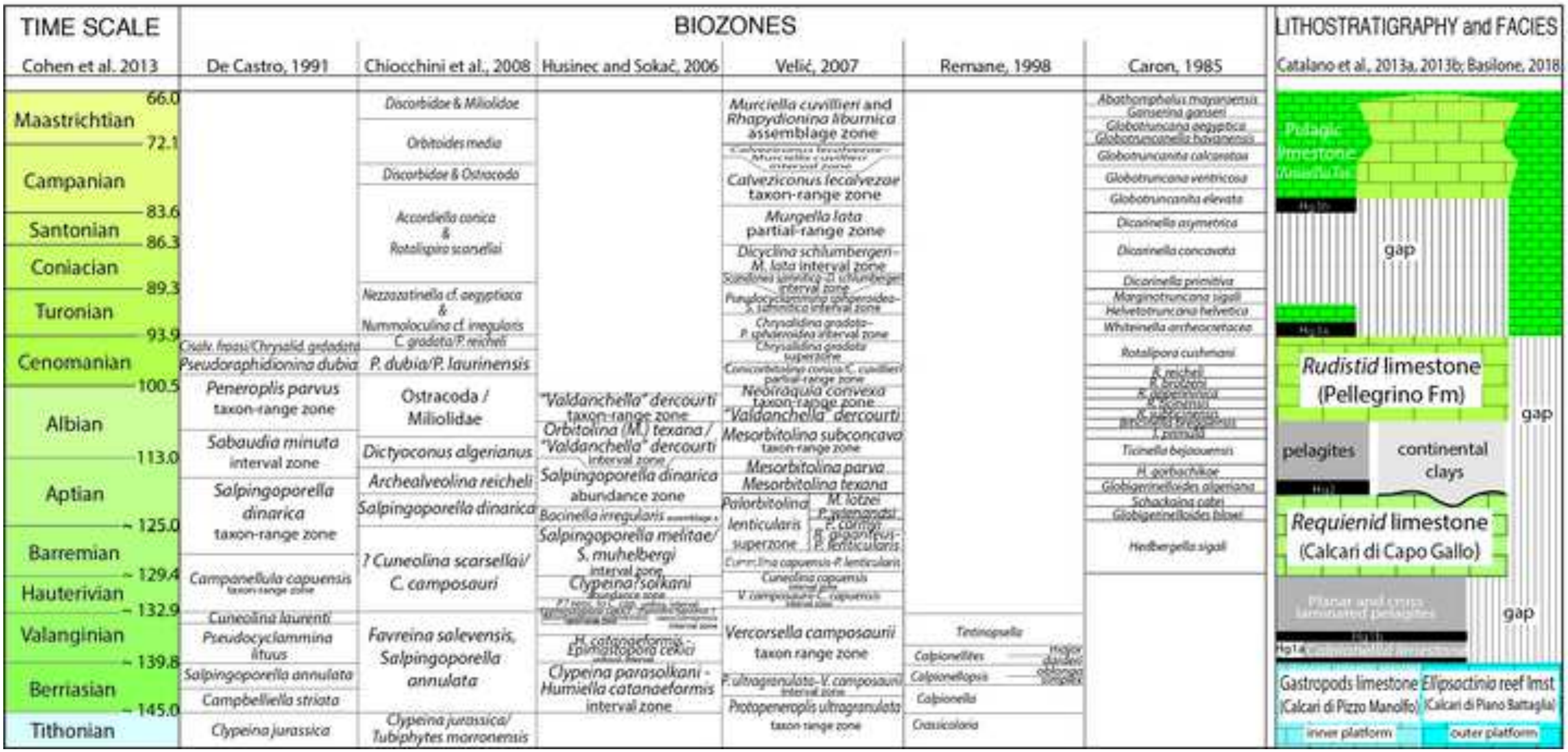

Figure 3 Click here to access/download;Figure;Fig. 3.tif

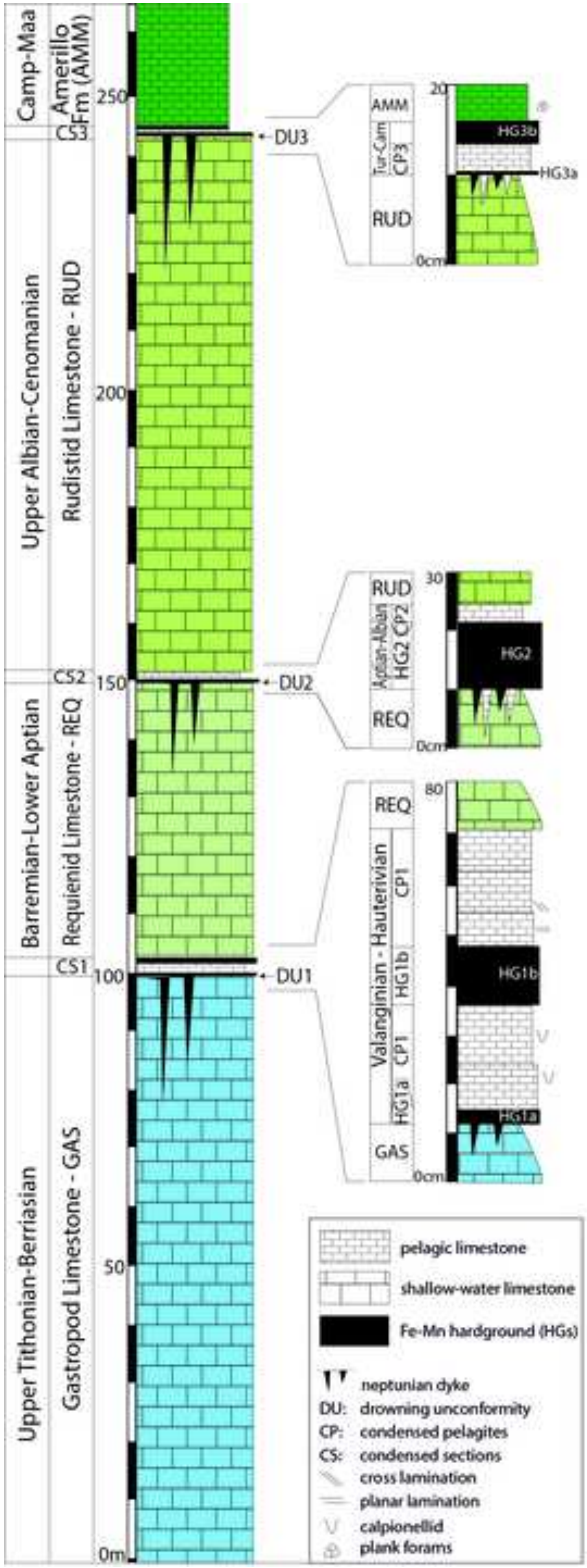

Figure 4 Click here to access/download;Figure;Fig. 4.tif

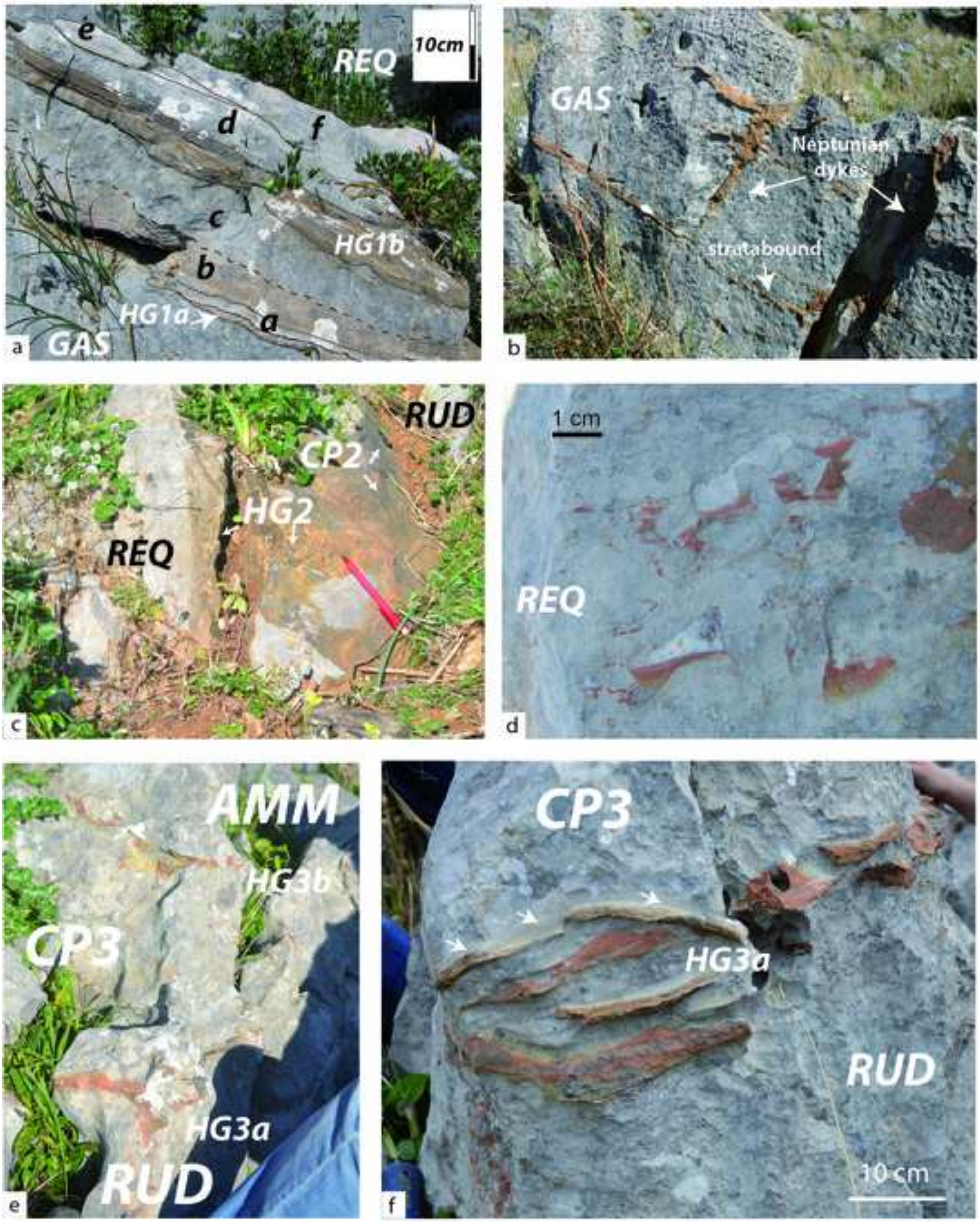

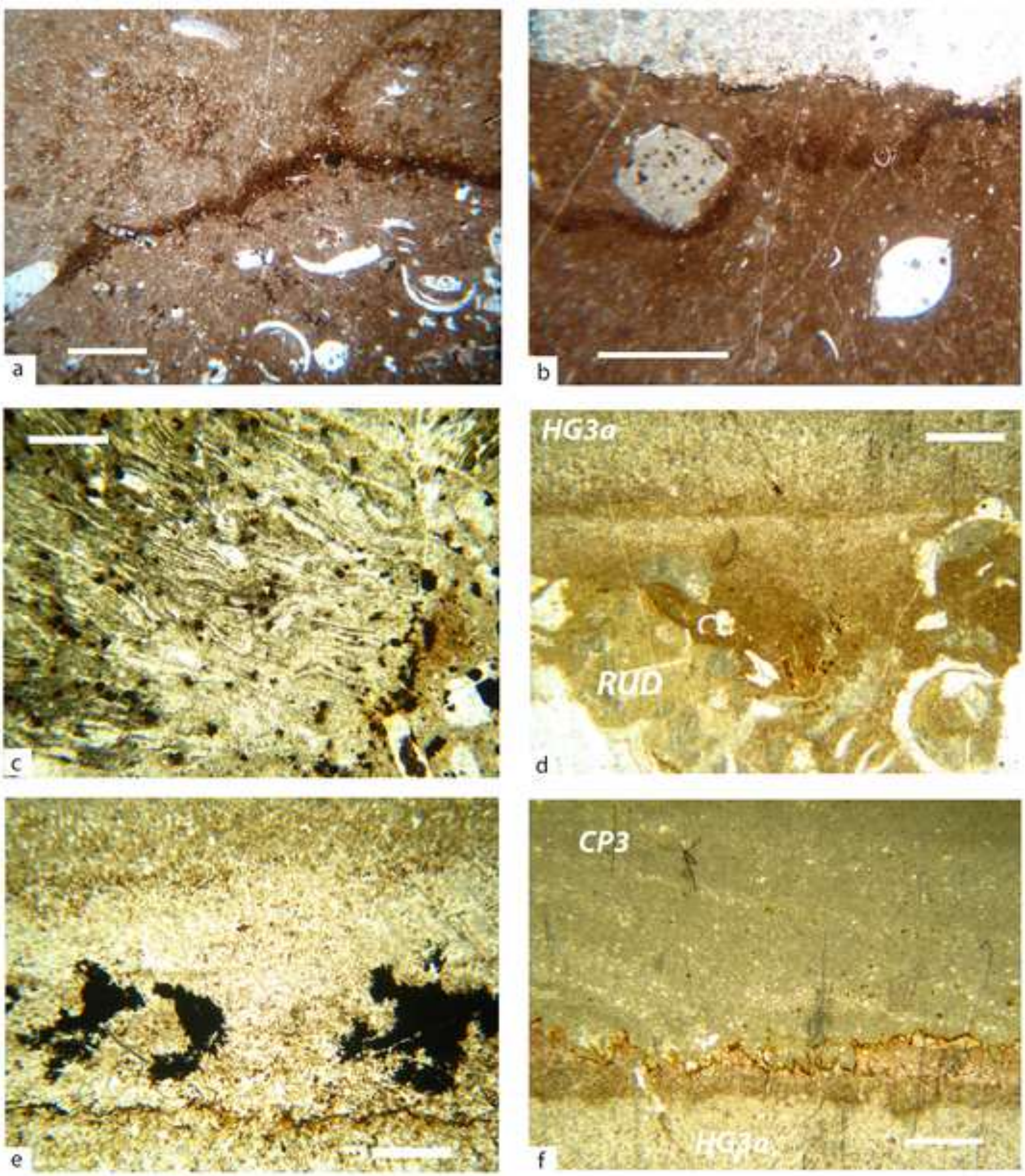
a
b
HG3a
RUD
c
d
CP3
e
f

Figure 6

Click here to access/download;Figure;Fig. 6.tif

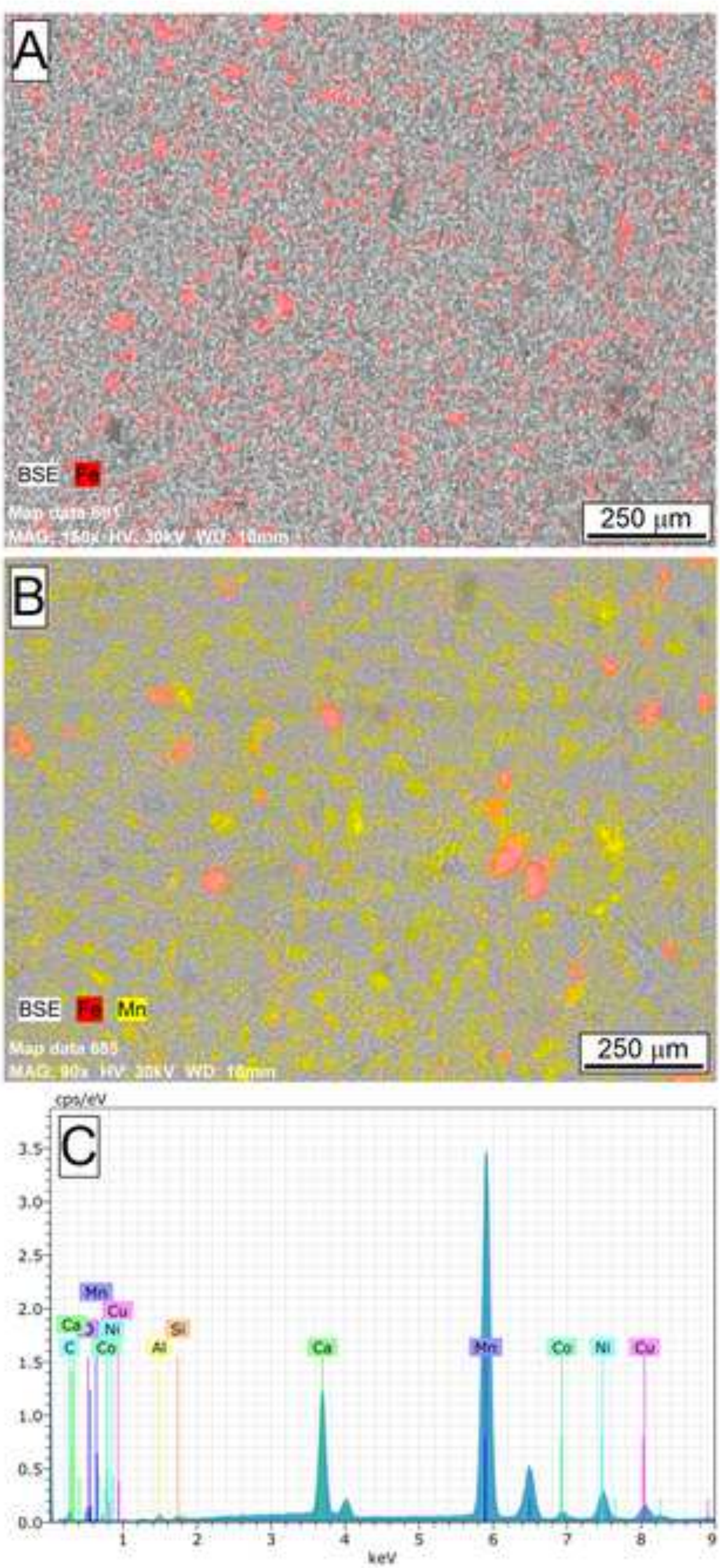

Figure 7

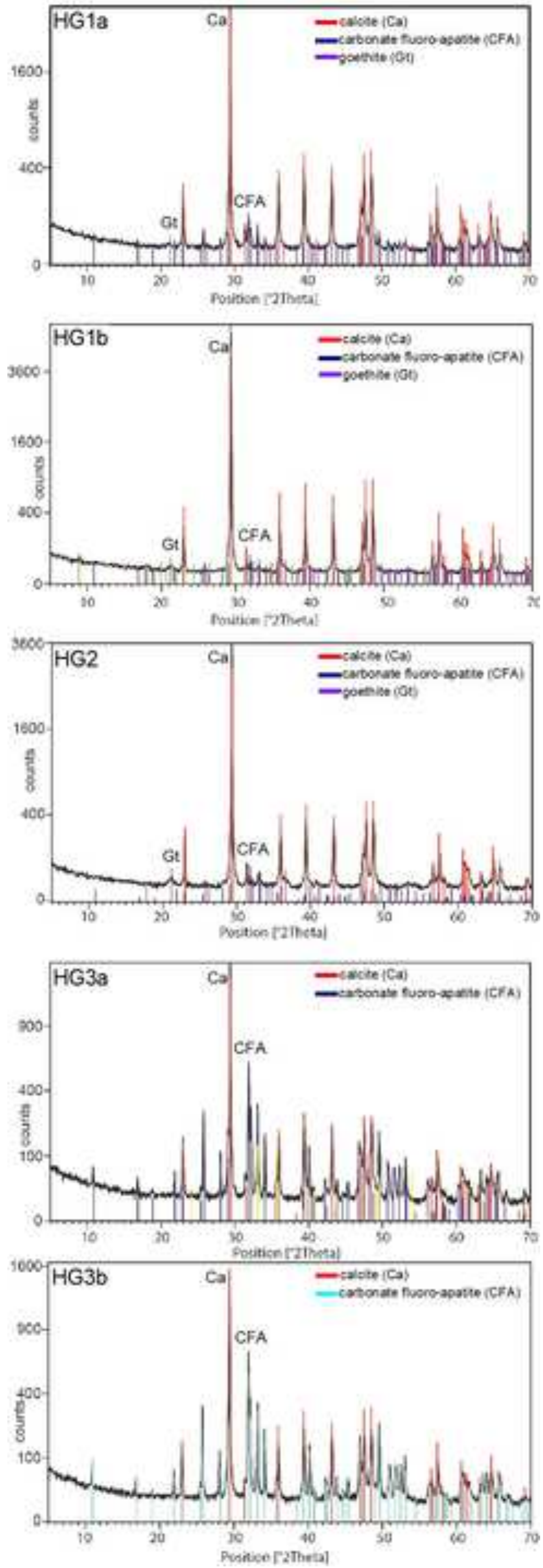

HG1a
Ca
CFA
Gt
calcite (Ca)
carbonate fluoro-apatite (CFA)
goethite (Gt)
counts
Position [°2Theta]
HG1b
HG2
HG3a
HG3b

Figure 8

Click here to access/download;Figure;Fig. 8.tif

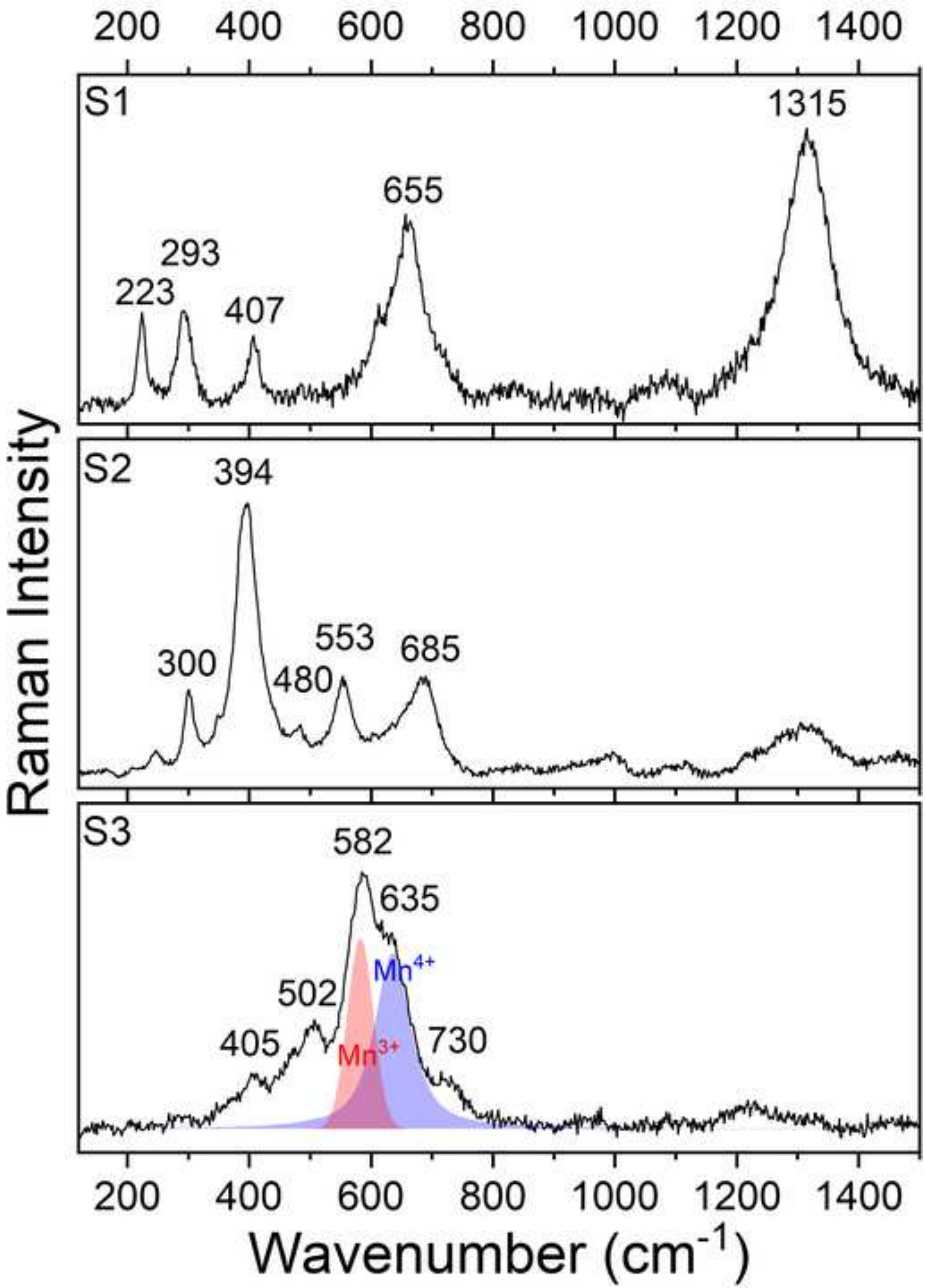

Figure 9

Click here to access/download;Figure;Fig. 9.tif

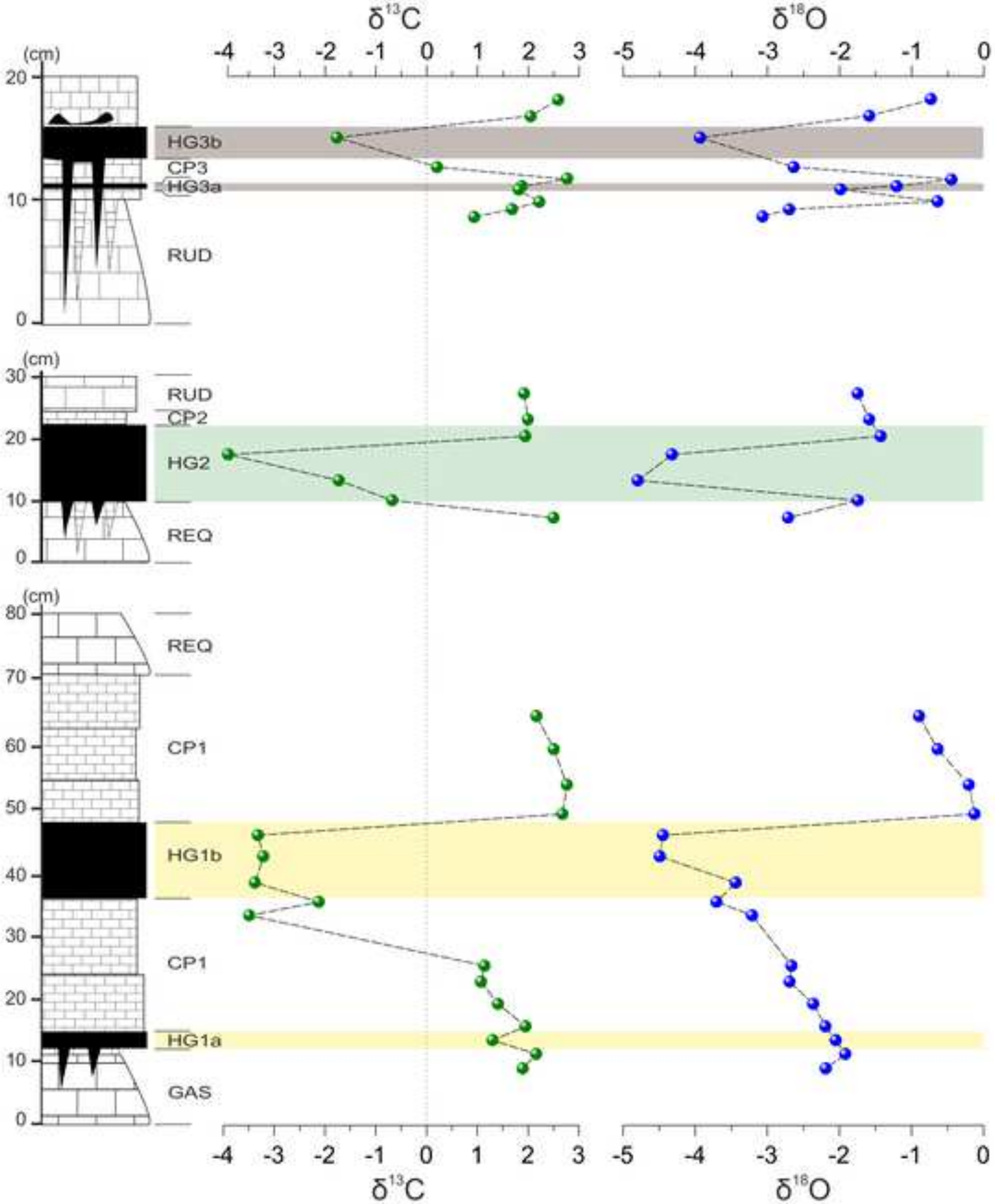

Figure 10

Click here to access/download;Figure;Fig. 10.tif

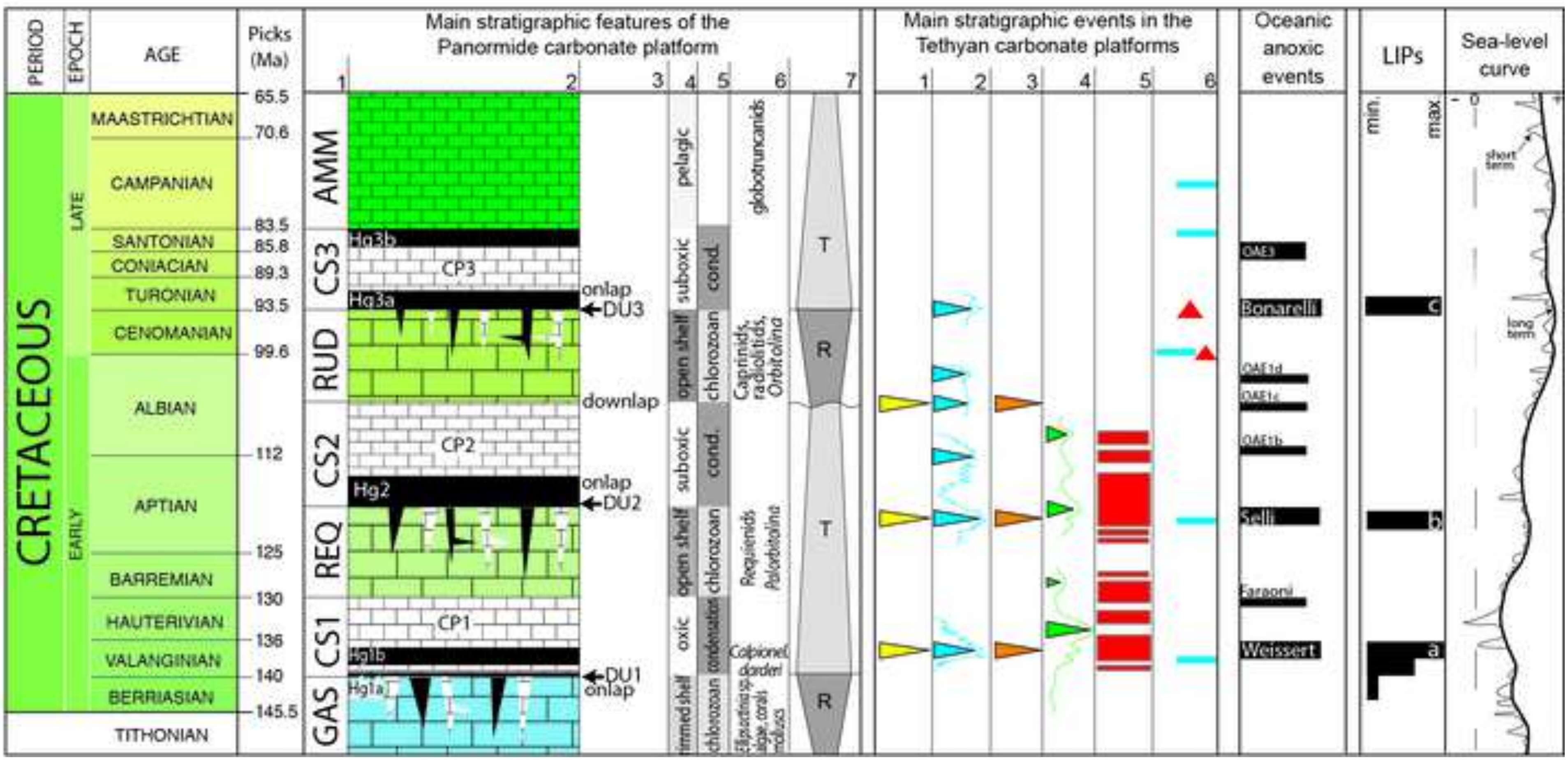

Figure 11

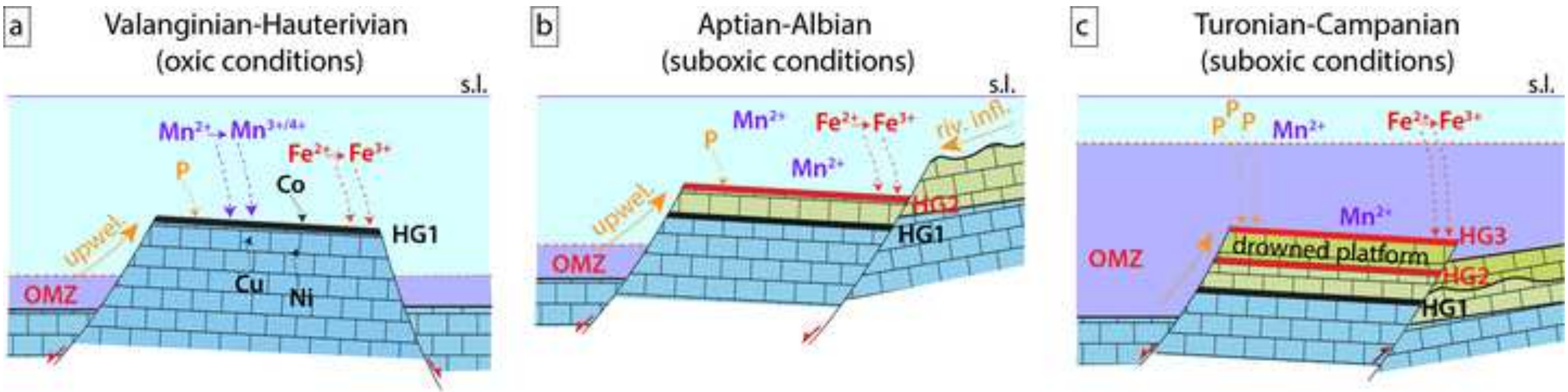
a
Valanginian-Hauterivian
(oxic conditions)
s.l.
Mn²⁺→Mn³⁺/⁴⁺
Fe²⁺→Fe³⁺
P
Co
HG1
upwel.
Cu
Ni
OMZ
b
Aptian-Albian
(suboxic conditions)
s.l.
Mn²⁺
Fe²⁺→Fe³⁺
P
riv. infl.
Mn²⁺
upwel.
HG2
HG1
OMZ
c
Turonian-Campanian
(suboxic conditions)
s.l.
P P P
Mn²⁺
Fe²⁺→Fe³⁺
Mn²⁺
HG3
OMZ
drowned platform
HG2
HG1

Table 1

Units	Texture and lithology	thick (m)	Fossil content	Lower boundary	Environment	Age	Main references
Amerillo Fm	red and white planktonic foraminifera bearing-wackestone and marly limestone with intercalation of resedimented bioclastic packstone/grainstone	1-10	*Globotruncana* ex gr. *lapparenti*, *Globotruncana ventricosa*	onlap infilling	pelagic	Campanian-Paleogene	
Drowning unconformity 3 (DU3)							
Rudistid Limestone	floatstone-to-wackestone with rudistid shells and large *Nerinea* sp., corals, corallinaceous algae, encrusting organisms (microbialites), microproblematics and crinoid fragments alternated to oolitic packstone-grainstone	100-150	caprinids (*Caprina schiosensis* Boehm, *Caprina carinata* Boehm) caprotinids (*Polyconites verneuilli* Bayle), hippuritids, large radiolitids (*Sauvagesia sp.*, *Radiolites sauvagesi* D'ombres-Firmas), benthic foraminifera (*Orbitolina (Conicorbitolina) conica* D'Archiac), microproblematics, algae, corals	downlap	open shelf with patch reefs	Upper Albian-Cenomanian	Montanari, 1965; Camoin, 1983
Drowning unconformity 2 (DU2)							
Requienid Limestone	thick bedded floatstone-rudstone with requienids and large *Nerinea* sp., corals, coated grains, benthic foraminifera, algae and microproblematics alternated to dm-thick graded darkish oolitic grainstone and coral boundstone (patch reefs).	20-100	requienids (*Offneria* sp.), algae (*Clypeina solkani* Sokac, *Epimastopora cekici* Radoičić, *Salpingoporella hasi* Conrad, Radoicic & Rey, *Triploporella* cf. *decastroi* Barattolo), benthic foraminifera (*Palorbitolina lenticularis* (Blumenbach), *P. praecursor* (Montanari), *Rectodyctioconus giganteus* Schroeder), *Bacinella irregularis* Radoicic, *Lithocodium aggregatum* Elliot	onlap	open shelf and sand bar	Barremian-Lower Aptian	Montanari, 1965; Camoin, 1983
Drowning unconformity 1 (DU1)							
Gastropod Limestone	thick bedded graded rudstone-floatstone with gastropods, colonial corals (patch reef) and chetetids, bioclastic wackestone with algae, oncoids and coated grains, graded oolitic and bioclastic packstone-grainstone	100-150	*Nerinea* sp., algae (*Cayeuxia* sp., *Clypeina jurassica* Favre & Richard, *Campbeliella striata* Carozzi, *Epimastopora cekici* Radoičić), benthic foraminifera (*Protopeneroplis striata* Weynschenk, *Trocholina* cfr. *elongata* Leupold), microproblematics (*Lithocodium aggregatum*, *Bacinella irregularis*), echinoids, crinoids bryozoans	onlap	lagoon and landward marine sand belt	Upper Tithonian-Lower Valanginian	Basilone and Sulli, 2016

Sample	Lithology and texture	Thick. (cm)	Stratigraphy	Major minerals	Minor minerals
HG1a	Brick-red to blackish massive and infilling fractures and sedimentary dykes	6 to 8	top of *Gastropods* limestone	Ca	CFA, Gt, He, Bi/Ve
HG1b	laminated black	8 to 12	interlayered in the CS1	Ca	CFA, Gt, He, Bi/Ve
HG2	brick-red to blackish massive, with infilling materials in neptunian dykes	10 to 20	top of *Requienid* limestone	Ca	CFA, Gt, He, Bi/Ve
HG3a	reddish to brick-red crust alternated with planktonic foraminifers-bearing grainstone and infilling neptunian dykes and dissolution cavities	4 to 6	top of *Rudistid* limestone	Ca, CFA	Gt, He
HG3b	reddish encrustations	1 to 3	top of CS3	Ca, CFA	Gt, He